

# Lawrence Berkeley National Laboratory

## LBL Publications

### Title

Effects of time-dependent deformation of shale on the integrity of a geological nuclear waste repository

### Permalink

<https://escholarship.org/uc/item/8pd5f757>

### Authors

Sasaki, Tsubasa

Rutqvist, Jonny

### Publication Date

2022-10-01

### DOI

10.1016/j.ijrmms.2022.105206

Peer reviewed

# Effects of time-dependent deformation of shale on the integrity of a geological nuclear waste repository

Tsubasa Sasaki <sup>a</sup> and Jonny Rutqvist <sup>a,\*</sup>

<sup>a</sup> Earth Sciences Division, Lawrence Berkeley National Laboratory, 1 Cyclotron Road, Berkeley, CA, 94720, USA

\* Corresponding author. E-mail address: jrutqvist@lbl.gov

## Highlights

- High shale creep improved formation integrity in the near field
- High shale creep also increased buffer compaction in the long term (> 1,000 years)
- In the shorter term, however, buffer compaction was greater with lower shale creep

## Abstract

Safety assessment of geological nuclear waste repositories is essential for the permanent disposal of spent nuclear fuels and high-level radioactive waste. The long-term integrity of the host rock as well as the engineered barrier system (e.g., bentonite buffer) surrounding nuclear waste canisters is of particular importance as decay heat from nuclear waste canisters, which will last over thousands of years, significantly disturbs the thermo-hydromechanical (THM) state of the repository. In this study, THM coupled simulations were carried out to investigate the effect of time-dependent deformation (i.e., creep) of shale on the long-term integrity of a generic subsurface nuclear waste repository. The Norton-Bailey

creep model, which is also known as the Lemaitre-Menzel-Schreiner model, was employed to simulate the power-law type creep that is observed in shales. The TOUGH-FLAC simulator was employed for the THM coupled modeling of the repository. The objective of this study is to assess the effect of creep in different shales (i.e., high creep shale vs. low creep shale) on long-term stress and permeability changes in the repository. Results show potential advantages of constructing repositories in the high creep shale, as deviatoric stress levels in the formation decreased to zero in 100 years since the emplacement of nuclear waste canisters and the permeability also decreased to the undamaged, intrinsic levels in 10,000 years. Also, mean effective stress levels in the bentonite buffer increased by 100% in the high creep shale case relative to the low creep shale case at 10,000 years due to creep-induced contraction of the nuclear waste disposal tunnel. However, in earlier periods (e.g., 1,000 years), the stress levels in the bentonite buffer were twice smaller in the high creep shale case than in the low creep shale case, which shows a tradeoff between the intermediate- (~1,000 years) and long-term (>10,000 years) compaction levels in the bentonite buffer depending on the creep characteristics of the host shale.

## **Keywords**

Nuclear waste disposal; Shale; Creep; Bentonite; Coupled processes; Geomechanics

## **1. Introduction**

Geological nuclear waste repositories are considered a permanent solution for the disposal of spent nuclear fuels and high-level radioactive wastes <sup>1</sup>. A key challenge toward realizing geological nuclear waste repositories is the safety assessment (SA) and performance assessment (PA). In the SA, the predicted consequences of any releases from the repository are compared against appropriate environmental and health safety standards, whereas in the PA, long-term behaviors of the isolation

barriers in the repository are evaluated. The PA quantifies the long-term behaviors of each component of the repository and estimates their impact on the overall containment performance for an extremely long period (e.g. 100,000 years).

Geological nuclear waste repositories isolate radioactive wastes from the biosphere with a multi-barrier system<sup>2</sup>. The multi-barrier system typically consists of the natural barrier (e.g., bedrock) and the engineered barrier system (EBS). The bedrock provides stable chemical and mechanical environments, which impede radionuclide transport if released. The EBS provides the same functionalities within the buffer, which also provides mechanical stability to the canister as well to the surrounding bedrock, which can be damaged by excavation<sup>3</sup>. The excavation damage zone (EDZ) could create transport paths for radionuclides from a waste package<sup>4</sup>. Thus, the evolution of the EDZ needs to be examined carefully for the long term.

The evolution of the EDZ and the surrounding intact bedrock is a highly thermo-hydromechanically (THM) coupled process<sup>5</sup>. For instance, decay heat emitted from the emplaced radioactive waste causes thermal expansion of the rock and pore fluids, which results in rock deformations and fluid flow. This coupled process may significantly change the properties of the EDZ during the post-closure period. For instance, coupled processes could induce (self-)sealing, which significantly decreases the effective hydraulic conductivity of the EDZ with time<sup>6</sup>. Other mechanisms based on coupled processes such as accelerated creep, disintegration of the rock, swelling, and shear could also decrease the hydraulic conductivity<sup>6</sup>. To evaluate the effects of these mechanisms on the containment performance of the repository, it is crucial to examine THM coupled processes carefully.

Coupled processes related to geologic disposal of nuclear wastes have been intensively studied at underground research laboratories <sup>7-11</sup>. Coupled THM experiments at underground research laboratories are used not only to study coupled processes but also to validate numerical models, which are the only viable means for the long-term PA of nuclear waste repositories. Previous modeling studies on geological nuclear waste repositories have indicated potential failure of the EDZ and compaction/expansion of the bentonite buffer <sup>12-14</sup>. Their results also showed that temperature changes in the repository will induce thermal pressurization and thermal stress development in the host rock. Thermal pressurization develops due to the thermal expansion of trapped pore fluids in the low permeability host rock. Similarly, thermal stress develops due to poroelastic expansion in a laterally confined host rock. This increase in horizontal stress can concentrate deviatoric stresses around tunnel opening <sup>14</sup>. Such deviatoric stress concentration may damage the host rock and increase its permeability.

In the aforementioned studies, however, the effect of time-dependent deformation (i.e., creep) of the formation was not considered. Creep tends to relieve high deviatoric stresses and it could therefore be effective in accommodating long-term thermal stresses during the post-closure period. These creep effects have been examined in modeling studies for salt formations <sup>15-17</sup>; creep was shown to help seal and heal the EDZ in salt. This is also expected to be the case, according to laboratory and field studies, for the EDZ in shale formations, as creep was found to decrease the permeability empirically <sup>10,18</sup>. However, effects of creep on key aspects of repository integrity, such as stress and permeability changes in the formation as well as on the compaction/expansion of the bentonite buffer, have not been examined carefully in the previous studies.

This research extends the abovementioned studies by incorporating temperature-dependent creep of shale into the THM coupled modeling of a geological nuclear waste repository. The primary objective is to assess the effect of creep on stress and permeability changes in shale formations as well as on the interaction between the formation and bentonite buffer during the long-term decay heating from nuclear waste canisters. Irrecoverable creep strains in shales have been found to follow the so-called power law from laboratory experiments<sup>19-23</sup>. The Norton-Bailey creep model, among other power-law creep models, is used in this study as this creep model is capable of modeling creep under low to intermediate deviatoric stress levels ( $< 60$  MPa)<sup>24</sup>, which is expected to develop in geological nuclear waste repositories. The Norton-Bailey model can also simulate temperature-dependent creep. As for the THM coupled modeling, the TOUGH-FLAC simulator<sup>25,26</sup> was used. Details of the THM coupled modeling as well as the creep constitutive model are provided in the following sections.

## **2. Numerical modeling**

### **2.1. Model geometry**

Figure 1 shows the geometry and boundary conditions of the TOUGH-FLAC model of a geological nuclear waste repository. The total depth and length of the model is 1,000 m and 50 m, respectively, with the disposal tunnel being located at the central depth (500 m) and length (25 m). The out-of-plane width of the model is 1 m. It is noted that the displacements in the out-of-plane direction were constrained so the model is effectively a 2D plane-strain model.

As to the mechanical boundary conditions, the displacements in the normal directions along the lateral boundaries (i.e.,  $x$ -direction) are constrained (i.e., the roller boundary) to represent a symmetry between adjacent disposal tunnels, which are assumed to be excavated in parallel to one another at a spacing of 50 m at the same depth. The normal displacements at the bottom boundary (i.e.,  $z$ -direction) are constrained

as well, whereas at the top boundary, a constant pressure of 0.1 MPa was applied to consider the effect of atmospheric pressure at the ground surface. The inner boundary of the canister (i.e., the inner surface of the canister elements) was applied with constant pressure of 0 MPa.

Regarding the thermo-hydraulic boundary conditions, no fluid flow or heat flux were allowed across the lateral boundaries as well as across the inner boundary of the canister, whereas constant pore pressure and temperatures of 0.1 MPa and 10°C and of 9.91 MPa and 40°C were specified on the top and bottom boundaries, respectively.

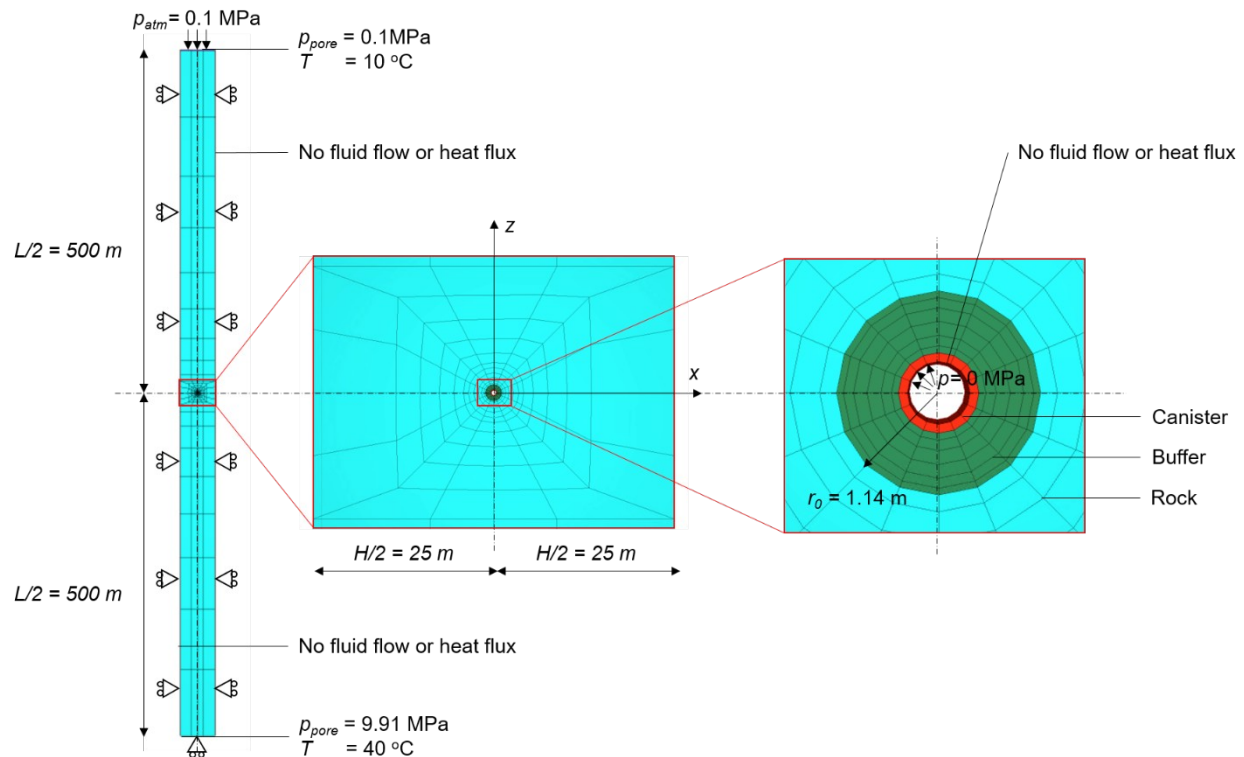


Figure 1 The geometry and boundary conditions of the model <sup>12</sup>.

## 2.2. Thermo-hydromechanically coupled modeling

The modeling of THM coupled behaviors of the repository was carried out with the TOUGH-FLAC simulator<sup>25,26</sup>, which consists of a multiphase fluid flow and thermal transport simulator, TOUGH3<sup>27</sup>, and a commercial finite difference software, FLAC3D<sup>28</sup>. TOUGH-FLAC is a semi-coupled simulator in a way that TOUGH3 is the master code, which handles the thermo-hydraulic (TH) calculations and passes the arrays of TH outputs to FLAC3D, which is the subordinate code that imports the TOUGH3 outputs, such as pore pressure, temperature, capillary pressure, etc., to compute mechanical outputs, such as displacements, stresses, and strains. The FLAC3D outputs are then used to update TOUGH3 parameters, such as permeability and porosity, and the simulation continues in this sequentially-coupled manner. It is noted that the coupling between TOUGH3 and FLAC3D is performed at each TOUGH3 timestep (i.e., sequentially explicit scheme<sup>25</sup>). The TOUGH-FLAC simulator was selected for this study since it has successfully simulated a wide variety of THM coupled phenomena in subsurface formations<sup>13,25,29</sup>.

The equation-of-state module #4 (EOS4), where the model components are water and air, which can be either in the liquid or gaseous state, was selected for TOUGH3. In the EOS4, the van Genuchten-Mualem relative permeability model and the van Genuchten capillary pressure function were selected as shown below.

$$k_{rl} = \begin{cases} \sqrt{S_l^i} \left( 1 - \left( 1 - (S_l^i)^{1/\lambda_k} \right)^{\lambda_k} \right)^2 & \text{if } S_l < S_{ls} \\ 1 & \text{if } S_l \geq S_{ls} \end{cases} \quad (1)$$

$$k_{rg} = \begin{cases} 1 - k_{rl} & \text{if } S_{gr} = 0 \\ (1 - \hat{S})^2 (1 - \hat{S}^2) & \text{if } S_{gr} > 0 \end{cases}$$

where

$$S_l^i = (S_l - S_{lr}) / (S_{ls} - S_{lr}) \quad (2)$$

$$\hat{S} = (S_l - S_{lr}) / (1 - S_{lr} - S_{gr}) \quad (3)$$

where  $k_{rl}$  is the relative permeability of the liquid phase (-),  $k_{rg}$  is the relative permeability of the gas phase (-),  $\lambda_k$  is a van Genuchten parameter (-) (in the original notation<sup>30</sup>,  $\lambda_k$  is expressed as  $m$ ),  $S_l$  is the



liquid-phase saturation (-),  $S_{lr}$  is the residual (i.e., minimum) liquid-phase saturation (-),  $S_{ls}$  is the saturated (i.e., maximum) liquid-phase saturation (-),  $S_{gr}$  is the residual gas-phase saturation (-) (it is noted that  $0 \leq k_{rl} \leq 1$  and  $0 \leq k_{rg} \leq 1$  were imposed), and

$$P_{cap} = -P_0 \left( (S^i)^{-1/\lambda_k} - 1 \right)^{1-\lambda_k} \quad (4)$$

where  $P_0$  is a parameter analogous to the air entry pressure (Pa). The maximum capillary pressure value,  $P_{max}$ , was specified such that  $-P_{max} \leq P_{cap} \leq 0$ .

148

Further details of TOUGH3 and EOS4 with regard to their implementation in the nuclear waste repository are provided in our previous work <sup>12</sup>. Hence, they are omitted herein and only the values of the TOUGH3 input parameters are provided below in Table 1. In the table, it can be seen that the canister was considered as a porous medium. This is because all materials are assumed to be porous in TOUGH3. In order to model nonporous medium such as steel, the porosity of such material is set to a very small value (e.g., 0.001), whereas the permeability is set to a comparable value to that of the neighboring material (e.g., bentonite) ( $2 \cdot 10^{-21} \text{ m}^2$ ) to avoid convergence issues at the interface. This did not affect the fluid flow or advective thermal flux calculations in the repository model because the total pore volume of the canister zones was negligible, i.e., orders of magnitude smaller than that of the rock and bentonite zones.

158

159 Table 1 The values of the TOUGH3 input parameters.

	Rock	Buffer	Canister
Grain density (kg/m <sup>3</sup> )	2700	2700	7800
Porosity (-)	0.15	0.41	0.001
Absolute permeability (m <sup>2</sup> )	$5 \cdot 10^{-20}$	$2 \cdot 10^{-21}$	$2 \cdot 10^{-21}$
Thermal conductivity (W/(m·°C))	2.2	1.26	12.0
Grain specific heat (J/(kg·°C))	900	800	500

Pore compressibility (1/Pa)	$1 \cdot 10^{-9}$	$5 \cdot 10^{-8}$	0
Pore expansivity (1/°C)	0	$1 \cdot 10^{-4}$	0
Diffusion coefficient for water vapor (m <sup>2</sup> /s)	$1.73 \cdot 10^{-5}$	$1.73 \cdot 10^{-5}$	$1.73 \cdot 10^{-5}$
van Genuchten parameter, $\lambda_k$ (-)	0.41	0.32	0.32
Residual liquid saturation for relative permeability, $S_{lr}$ (-)	0.2	-	-
Residual liquid saturation for capillary pressure, $S_{lr}$ (-)	0.1	0.1	0.1
Saturated liquid saturation, $S_{ls}$ (-)	1.0	1.0	1
Residual gas saturation, $S_{gr}$ (-)	0.01	0	0
Capillary pressure parameter, $P_0$ (Pa)	$4.76 \cdot 10^7$	$3 \cdot 10^7$	$3 \cdot 10^7$
Maximum capillary pressure, $P_{max}$ (Pa)	$1 \cdot 10^8$	$5 \cdot 10^9$	$5 \cdot 10^9$

### 2.3. Mechanical constitutive models

Constitutive models are central to the modeling of mechanical behaviors of solid. Herein the details of the constitutive models of the model components (i.e., rock, bentonite buffer, and canister) that were implemented in FLAC3D are provided. The rock was modeled as a viscoplastic material by employing a power-law creep model, whereas the bentonite buffer and canister were modeled as time-independent materials as described in the following sections.

#### 2.3.1. Formation

It has been experimentally demonstrated that creep deformations of shales follow the so-called power law <sup>19–22,24,31–34</sup>. The main mechanism of power-law creep in shales seems to be pressure solution at grain contacts <sup>35</sup>; it is not caused by hydromechanical coupling, friction sliding between grains, or sub-critical crack growth <sup>36</sup>. The power-law creep can be expressed in terms of elastic ( $J_{elastic}$ ) and creep ( $J_{creep}$ ) compliances as shown below (in the case of axial creep):

$$J = \Delta \epsilon / \Delta \sigma = J_{elastic} + J_{creep} = 1/E + A_J \left( t/t_{ref} \right)^m \quad (5)$$

where  $\Delta \epsilon$  is the axial strain increment (-),  $\Delta \sigma$  is the deviatoric stress increment (Pa),  $E$  is Young's modulus (Pa),  $A_J$  is a power-law coefficient ( $\text{Pa}^{-1}$ ),  $m$  is a power-law exponent (-),  $t$  is the time (s), and  $t_{ref}$  is a reference time (s) ( $= 1$ ) for the normalization of  $t$ . The values of  $A$  and  $m$  can be stress- and/or temperature-dependent<sup>23,31</sup> and the value of  $m$  is usually less than unity for shales<sup>19,36</sup>, which indicates that the power law is suitable for the modeling of the primary creep as the creep strain rate under  $m < 1$  decreases monotonically with time.

The above power law is expressed in the simplest form and cannot be applied under more complex loading conditions where, for example, the values of all six stress tensor components change with time. In such cases, a generalized version of the power law is necessary. The Norton-Bailey law<sup>37,38</sup> is one of such creep models and it can be expressed as follows<sup>39</sup>:

$$\dot{\epsilon}_{cr,ij} = F_{cr} m \left( \left( \epsilon_{cr,e} + \epsilon_{shift} \right) / \left( t_{ref} F_{cr} \right) \right)^{(m-1)/m} n_{D,ij} \quad (6)$$

where

$$F_{cr} = A \cdot \exp \left( -Q/(RT) \right) \left( \sigma_e / \sigma_{ref} \right)^n \quad (7)$$

$$n_{D,ij} = (3/2) \left( \sigma_{ij}^d / \sigma_e \right) \quad (8)$$

$$\epsilon_{cr,e} = \int \dot{\epsilon}_{cr,e} dt = \int \sqrt{(2/3)} \dot{\epsilon}_{cr,ij} : \dot{\epsilon}_{cr,ij} dt \quad (9)$$

where  $\dot{\epsilon}_{cr,ij}$  is the creep strain rate tensor (-),  $m$  is the power-law exponent (-),  $\epsilon_{shift}$  is an effective creep strain shift (-),  $\epsilon_{cr,e}$  is the effective creep strain (-),  $\dot{\epsilon}_{cr,e}$  is the effective creep strain rate ( $s^{-1}$ ),  $\sigma_{ij}^d$  is the deviatoric stress tensor (Pa),  $\sigma_e$  is von Mises effective stress (Pa),  $A$  is a power-law coefficient ( $s^{-1}$ ),  $n$  is a power-law exponent (-),  $\sigma_{ref}$  is a reference stress (Pa),  $t_{ref}$  is a reference time (s) (= 1),  $Q$  is apparent activation energy (J/mol),  $T$  is the absolute temperature, and  $R$  is the gas constant (= 8.3145 J/mol/K). The Norton-Bailey law can be interchangeably referred to as the Lemaitre-Menzel-Schreiner (LMS) law<sup>40,41</sup>, as the formula of the Norton-Bailey law shown in Eq. (6) and that of the LMS law, such as the one presented as the Eq. (1) in Kazmierczak et al. (2007)<sup>42</sup>, are equivalent to each other. Also, the power-law coefficient  $A_J$  in Eq. (5) and  $A$  in Eq. (7) are equivalent to each other as shown below; the time derivative of Eq. (5) is:

$$\dot{\epsilon}_{creep} = \left( dJ_{creep}/dt \right) \Delta\sigma = \sigma_{ref} \left( A_J/t_{ref} \right) m \left( t/t_{ref} \right)^{m-1} \left( \Delta\sigma/\sigma_{ref} \right) \quad (10)$$

where  $\sigma_{ref}$  is a reference stress (Pa) (= 1), whereas a time-hardening version of the Norton-Bailey law can be expressed as follows<sup>39</sup>:

$$\dot{\epsilon}_{creep} = A m \left( t/t_{ref} \right)^{m-1} \left( \Delta\sigma/\sigma_{ref} \right) \quad (11)$$

Hence,  $A = \sigma_{ref} \left( A_J/t_{ref} \right)$ ; the values of  $A_J$  and  $A$  are identical but they have different units ( $Pa^{-1}$  for  $A_J$  and  $s^{-1}$  for  $A$ ). A visual interpretation of  $A_J$  is that it becomes the intercept of a log(time) vs. log(creep compliance) curve at  $t = 1$  s, which is shown later in Figure 2b. Lastly,  $\epsilon_{shift}(0)$  is introduced in Eq. (6) to guarantee a finite creep strain increment at the initiation of creep (i.e., to calculate  $\dot{\epsilon}_{cr,ij}$  when  $\epsilon_{cr,e} = 0$ ).

The above formulae of the Norton-Bailey model have been implemented in FLAC3D via a user-defined constitutive model. The model was verified through a one-element simulation where a cube element with a side length of 10 cm was subjected to axial loads. The vertical displacement at the bottom boundary was fixed while a confining stress of 10 MPa was applied on the lateral boundaries. The axial load of 10 MPa was applied on the top boundary, which was then increased instantaneously to 20 MPa. The simulation was run for a period of approximately two weeks and the change in the axial strain was computed. The assigned elastic and creep material properties, which were obtained from experimental data on shales<sup>19</sup>, are listed in Table 2. The table lists two types of shale (i.e., high and low creep shales), in which the high creep shale contains a much higher amount of clay minerals (~40%) than the low creep shale (~20%). Note that the temperature dependence of the creep is not considered in this verification simulation (i.e.,  $Q = 0$ ). The values shown in the parentheses are those for the main simulation, where the temperature-dependence was incorporated, for the repository modeling described later.

Table 2 The values of the Norton-Bailey model input parameters.

	High creep shale	Low creep shale
Young's modulus, $E$ (GPa)	13.889	35.765
Poisson's ratio, $\nu$ (-)	0.195	0.318
	$1.11 \cdot 10^{-15}$	$6.43 \cdot 10^{-14}$
Power-law coefficient, $A$ ( $s^{-1}$ )	$(1.60 \cdot 10^{-13})$	$(9.27 \cdot 10^{-12})$
Power-law exponent, $m$ (-)	0.716	0.262
Power-law exponent, $n$ (-)	1.0	1.0
Reference stress, $\sigma_{ref}$ (Pa)	1	1
Reference time, $t_{ref}$ (s)	1	1
Strain shift, $\epsilon_{shift}$ (-)	$1 \cdot 10^{-12}$	$1 \cdot 10^{-7}$
	0	0
Activation energy, $Q$ (kJ/mol)	(15)	(15)
Linear thermal expansion		
coefficient ( $1/^{\circ}C$ )	$1.0 \cdot 10^{-5}$	$1.0 \cdot 10^{-5}$

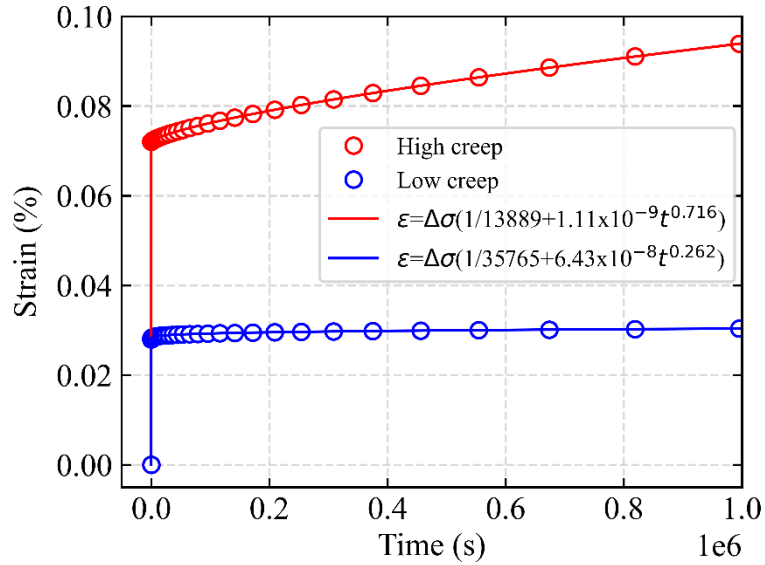
Figure 2 shows results of the verification simulation. The dots represent the numerical results, whereas the lines the analytical solutions obtained from the power law formula provided in Eq. (5) with the same parameter values for  $E$ ,  $A$ , and  $m$  as shown in Table 2 as well as  $\Delta\sigma = 10$  MPa. They were in good agreement with each other, except for the low creep result in Figure 2b at  $t < 1$  s. It was found that the error was controlled by the value of  $\epsilon_{shift}$ ; smaller  $\epsilon_{shift}$  values than the selected value of  $10^{-7}$  (e.g.,  $10^{-12}$ ) eliminated the error but they caused numerical convergence issues in the repository-scale simulation, whereas larger values rendered the error propagate to the longer time domain ( $t > 1$  s). Hence, the value of  $10^{-7}$  was used for the low creep shale case. This is reasonable because the error in creep strains at  $t < 1$  s would not affect the calculations for the simulated timeframe of  $\sim 10,000$  years in the repository. Also, it is noted that the creep strain in the low creep case remained significantly small relative to its elastic strain because of the short period of the verification simulation ( $\sim 12$  days). However, this would not be the case if a much longer period was simulated (e.g.,  $> 10,000$  years in the repository).

Figure 3 shows results of the simulation under a step load, where the axial load was initially kept at 10 MPa (i.e., zero deviatoric stress) for roughly 0.72 years and then set to 20 MPa (i.e., 10 MPa deviatoric stress) for another 0.72 years. The duration was arbitrary but long enough to induce creep. The results show the importance of employing the strain-hardening formula of the Norton-Bailey creep model in changing stress conditions, as the time-hardening formula shown below<sup>39</sup> developed errors especially in the high creep shale case.

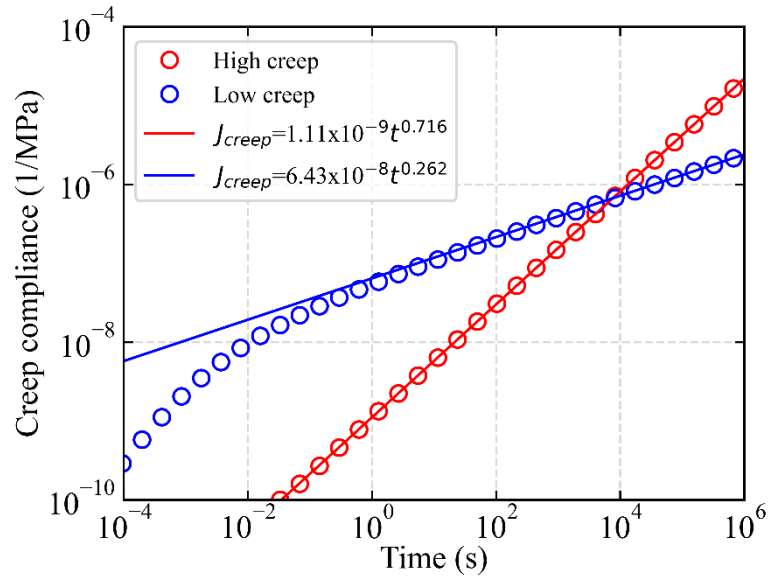
$$\dot{\epsilon}_{cr,ij} = F_{cr} m \left( (t + t_{shift}) / t_{ref} \right)^{m-1} n_{D,ij} \quad (12)$$

where  $t$  is the time (a state variable in this formulation), and  $t_{shift}$  is the time shift for preventing infinite creep strains at  $t = 0$  (the values of  $10^{-7}$  s and  $10^{-12}$  s were used for the low and high creep cases, respectively; these values are identical to those of  $\epsilon_{shift}$ , as  $t_{shift}$  corresponds to  $\epsilon_{shift}$ ). The errors in the

time-hardening formulation developed because the time variable continued increasing even when the deviatoric stress was zero during the first 0.72 years, whereas no such errors occurred in the strain-hardening formulation. This is because the effective creep strain ( $\epsilon_{cr,e}$ ), which is a state variable in the strain-hardening formula (corresponding to  $t$  in the time-hardening formulation), does not increase when the deviatoric stress remains at zero. This feature is essential in the modeling of creep in nuclear waste repositories as the stress levels in the formation change over an extremely long period.



(a)



(b)

Figure 2 Simulation results under a constant axial load: (a) time vs. axial strain; (b) time vs. creep compliance.

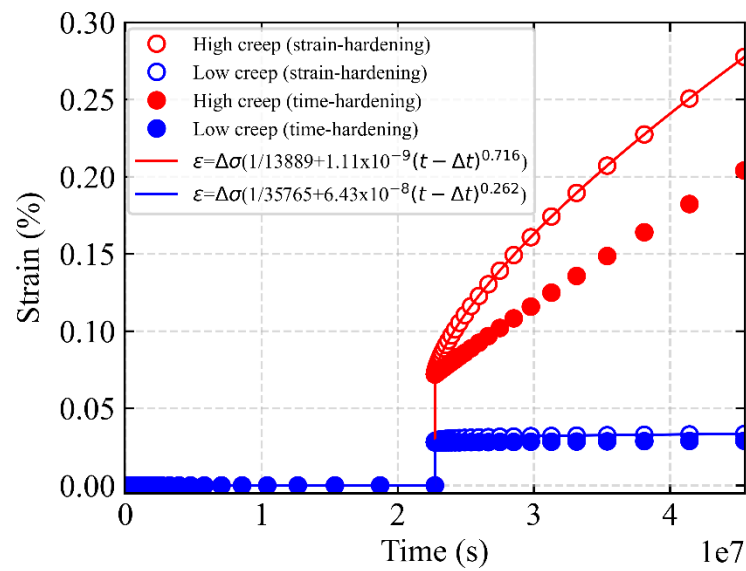


Figure 3 Simulation results under an axial step load.



### 2.3.2. Bentonite buffer

Barcelona Basic model (BBM) <sup>43</sup> was used to model the mechanical behaviors of the bentonite buffer, as this model is capable of simulating the swelling of unsaturated clays, which is expected to occur in the buffer during the post-closure period. BBM was implemented as a user-defined constitutive model in FLAC3D. The details of this model are provided in <sup>44</sup> and hence only the essential formulae of the BBM are presented herein. First, the elastic behavior of the BBM is modeled as follows.

$$d\epsilon_{vp}^e = (\kappa_p / v p') dp' \quad (13)$$

$$d\epsilon_{vs}^e = (\kappa_s / (v(s + p_{amt}))) ds \quad (14)$$

$$d\epsilon_q^e = (1 / (3G)) dq \quad (15)$$

where  $d\epsilon_{vp}^e$  is the elastic volumetric strain increment due to stress changes,  $d\epsilon_{vs}^e$  is the elastic volumetric strain increment due to suction (i.e., positive capillary pressure) changes,  $d\epsilon_q^e$  is the deviatoric strain increment,  $\kappa_p$  and  $\kappa_s$  are nonlinear stiffnesses (functions of  $s$  and  $p'$ ),  $G$  is the shear modulus,  $v$  is the specific volume,  $s$  is the suction,  $p_{amt}$  is the atmospheric pressure,  $p'$  is the mean effective stress,  $dp'$  is the mean effective stress increment,  $ds$  is the suction increment, and  $dq$  is the von Mises stress (i.e., deviatoric stress) increment.

Second, the yield locus of the BBM is defined as follows.

$$q^2 - M^2(p' + ks)(p_0 - p') = 0 \quad (16)$$

where  $M$  and  $k$  are constants, and  $p_0$  is an apparent pre-consolidation pressure, which is a function of the pre-consolidation pressure,  $p_0^i$ .

282 Third, the flow rule of the BBM is defined as follows.

$$d\epsilon_q^p/d\epsilon_{vp}^p = 2\alpha l \left( M^2 (2p' + ks - p_0) \right) \quad (17)$$

283

284 where  $d\epsilon_q^p$  is the equivalent plastic deviatoric strain increment,  $d\epsilon_{vp}^p$  is the plastic volumetric strain  
285 increment, and  $\alpha$  is a non-associated flow rule parameter.

286 Lastly, the hardening rule for the pre-consolidation pressure,  $p_0$ , is specified as follows.

$$dp_0/d\epsilon_v^p = \left( \nu l (\lambda_{p,s=0} - \kappa_p) \right) d\epsilon_v^p \quad (18)$$

287

288 where  $dp_0$  is the pre-consolidation pressure increment,  $\lambda_{p,s=0}$  is a non-linear plastic stiffness with respect  
289 to stress changes at  $s = 0$ , and  $d\epsilon_v^p$  is the total plastic volumetric strain increment. The input parameter  
290 values of the BBM are provided in Table 3, which were adopted from the previous calibration results of  
291 the BBM, which is based on the behavior of an unsaturated bentonite clay in the FEBEX in situ heater  
292 test at the Grimsel Test Site, Switzerland <sup>45</sup>.

293

294 Table 3 The values of the BBM input parameters.

	Buffer
Poisson's ratio (-)	0.4
Gradient of swelling line for stress, $\kappa_p$ (-)	0.05
Gradient of swelling line for suction, $\kappa_s$ (-)	0.25
Swelling gradient adjusting parameter, $\alpha_p$ (1/Pa)	$-3.0 \cdot 10^{-9}$
Swelling gradient adjusting parameter, $\alpha_s$ (-)	-0.161
Reference pressure, $p_{ref}$ (Pa)	$0.01 \cdot 10^6$

Gradient of compression line for stress, $\lambda_p^i$ (-)	0.15
Gradient of compression line for suction, $\lambda_s^i$ (-)	0.5
Compression gradient adjusting parameter, $r$ (-)	0.925
Compression gradient adjusting parameter, $\beta$ (1/Pa)	$0.1 \cdot 10^{-6}$
Tensile strength gradient, $k$ (-)	0.1
Reference mean net stress, $p^c$ (Pa)	$0.5 \cdot 10^6$
Critical state frictional constant, $M$ (-)	1.0
Pre-consolidation mean net stress, $p_0^i$ (Pa)	$12.0 \cdot 10^6$
Non-associated plastic flow parameter, $\alpha$ (-)	0.53
Linear thermal expansion coefficient (1/°C)	$1.5 \cdot 10^{-4}$

---

### 2.3.3. Canister

The linear isotropic elastic constitutive model was used to simulate the mechanical behaviors of the canister. Only two elastic parameters, namely Young's modulus and Poisson's ratio, control the behavior of this model and the values of 200 GPa and 0.3 were assigned, respectively. The linear thermal expansion coefficient of the canister was set to  $1.0 \cdot 10^{-5}$  (1/°C).

## 2.4. Simulation steps

### 2.4.1. Initial conditions

The initial TH conditions were obtained by running a TOUGH3 simulation until an equilibrium was achieved with constant pressure and temperature values set at the top (0.1 MPa and 10°C) and bottom (9.91 MPa and 40°C) boundaries. This resulted in a fully saturated model domain with linear pressure and temperature gradients of 9.81 kPa/m and 0.03°C/m, respectively. The initial mechanical conditions were

directly specified in FLAC3D with isotropic geostatic stresses ( $\sigma_{xx} = \sigma_{yy} = \sigma_{zz} = \rho g z$ ,  $\tau_{xy} = \tau_{yz} = \tau_{xz} = 0$ ), whereas the mechanical equilibrium was obtained in the following tunneling stage described below.

#### 2.4.2. Tunneling

The tunneling stage was simulated by TOUGH-FLAC in a THM coupled manner. The bentonite buffer and canister elements were assumed to represent the air inside the disposal tunnel during this stage, i.e. the buffer and canister elements were assigned with fictitiously small stiffness values (i.e., Young's modulus of  $1 \cdot 10^{-3}$  Pa and Poisson's ratio of 0.0) so that they would not affect the stress development of the surrounding formation. Also, constant gas pressure, gas saturation, and temperature of 0.1 MPa, 0.99, and 25°C were assigned to these elements and the fluid flow across the formation-buffer boundary was allowed. Note that during this stage the mechanical behavior of the buffer was modelled by the linear isotropic elastic constitutive model (i.e., identical to the one used for the canister). The tunneling stage was simulated for a period of 1.5 years and the values of the output variables (e.g., gas pressure, gas saturation, temperature, stresses, etc.) were used as the initial conditions in the following post-closure stage described below.

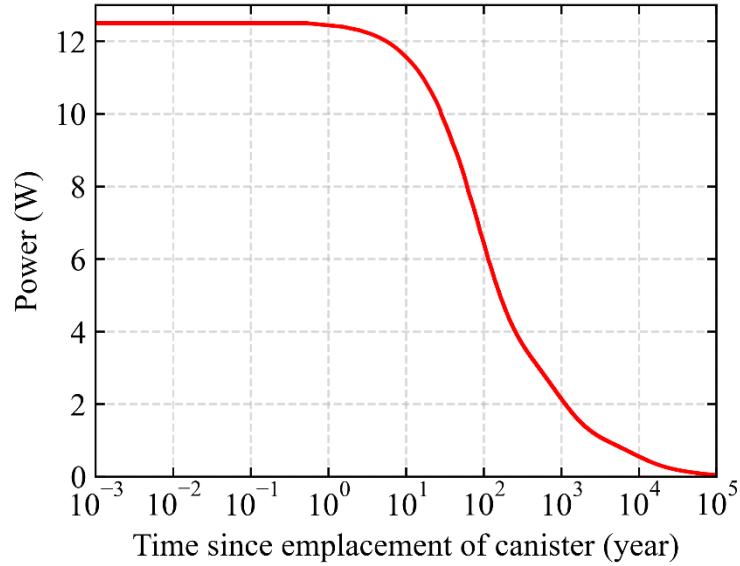
#### 2.4.3. Post-closure

At the beginning of the post-closure stage, the mechanical constitutive model of the bentonite buffer was changed to Barcelona Basic model (BBM) and the initial isotropic stress levels of 0.20 MPa ( $\sigma_{xx} = \sigma_{yy} = \sigma_{zz} = 0.20$  MPa,  $\tau_{xy} = \tau_{yz} = \tau_{xz} = 0$  MPa) were assigned. It is noted that the initial compressive stresses were given to the bentonite and canister zones, because, in an actual situation, the bentonite around the canister is compacted so that there is no gap between the bentonite and rock/canister, which also gives rise to the initial compressive stresses in the canister. The value of 0.2 MPa was arbitrary and it is an assumption

that the compressive stresses are isotropic. The validity of the value and the isotropic assumption may be examined in future studies. Also, the values of Young's modulus and Poisson's ratio of the canister were changed to 200 GPa and 0.3, respectively. The abovementioned initial isotropic stress levels for the buffer were assigned to the canister as well. Before the start of the TOUGH-FLAC simulation, the mechanical equilibrium was obtained in FLAC3D under the updated mechanical parameter and stress values. Thus, this represents an instantaneous installation of the waste canister and buffer into the waste emplacement tunnel.

To start the TOUGH-FLAC simulation, the gas pressure, gas saturation, and temperature of the buffer and the canister were set to the initial values of 0.1 MPa, 0.35, and 25°C, respectively, and the power emitted by each canister element was specified as a function of time as shown in Figure 4. This radioactive decay power function represents nuclear waste packages, each containing four PWR (pressurized water reactor) spent fuels, which are placed at a center-to-center spacing of 9 m between each waste package along the axis of the disposal tunnel after 60 years of interim storage. The initial power of the nuclear waste packages is assumed to be 200 W/m along the tunnel axis, which is equally divided into each of the 16 canister elements to obtain 12.5 W/m per canister element as shown in Figure 4.

348



349

350 Figure 4 Power decay function assigned to the canister elements <sup>12</sup>.

351

## 352 2.5. Simulation cases

353 The power-law parameters of shales are predominantly correlated with their clay and organic content (i.e.,  
354 the greater the clay and organic content in shale is, the greater its creep deformations become) <sup>18,46,47</sup>. The  
355 clay and organic content are also inversely correlated with elastic properties such as Young's modulus  
356 <sup>34,48</sup>. These indicate that shales can be broadly categorized as either creep-prone, low-stiffness shale or  
357 creep-resistant, high-stiffness shale. In this study, the former is referred to as the high creep shale,  
358 whereas the latter the low creep shale, and their representative elastic and power-law creep parameters  
359 were obtained from a laboratory experiment in the literature <sup>19</sup>.

360 The properties of the Norton-Bailey creep model for these shale cases are provided earlier in Table 2. In  
361 the simulation of the nuclear waste repository, the temperature dependence of the creep strain rate was  
362 activated by assigning  $Q = 15$  kJ/mol in Eq. (7) (i.e.,  $F_{cr} = A \cdot \exp(-Q/(RT)) \cdot (\sigma_e/\sigma_{ref})^n$ ). This value was

selected since the mean value of  $Q$  for the shear-induced creep of shales could range between 13 kJ/mol and 18 kJ/mol according to laboratory experiments<sup>31,49</sup>. It is noted, however, that the value of  $Q$  is significantly affected by multiple factors including the creep mechanism (e.g., pressure solution, microfracture development, etc.), the mineral components of shale, pressure and temperature conditions, etc. The power-law coefficient,  $A$ , needed to be modified as a result of the introduction of the temperature dependence term (i.e.,  $A \cdot \exp(-Q/(RT))$ ); the values of  $A$  of  $1.11 \cdot 10^{-15}$  and  $6.43 \cdot 10^{-14}$  for the high and low creep shales, respectively, were obtained from an experiment conducted at 90°C<sup>19</sup>. Hence, the values of  $A$  were respectively adjusted to  $1.60 \cdot 10^{-13}$  and  $9.27 \cdot 10^{-12}$  so that the experimental values are reproduced at 90°C.

### 3. Results

Results of the simulation for the post-closure period for the high and low creep shale cases are presented below. Changes in TH variables in the formation are presented first, followed by changes in formation stresses and permeability and how they are affected by creep. The effect of formation creep on changes in buffer stresses is also presented.

#### 3.1. Pore pressure and temperatures in the formation

Figure 5 shows changes in pore pressure, temperatures, and liquid saturation in the formation during the post-closure period when heat is released from the waste canister. The locations of the data readouts (e.g., V1, H1, etc.) in the figure correspond to those shown in Figure 6. It was found that formation creep had no significant impact on the pore pressure and temperatures changes (i.e., solid and dashed lines in Figure

385 5 overlap each other). This is because creep-induced permeability and/or porosity changes were too small  
 386 and too slow to affect fluid flow and heat flux calculations.

387 Temperatures around the disposal tunnel increased gradually from the initial value of approximately 25°C  
 388 to the maximum value of roughly 70°C at 100 years, whereas pore pressure remained at the initial levels  
 389 of nearly 0 MPa until about 10 years and then increased to the maximum value of slightly over 9 MPa at  
 390 1,000 years. The temperature changes were steady due to the small thermal conductivity of shale, while  
 391 the pore pressure changes were delayed as the formation around the disposal tunnel was initially  
 392 unsaturated due to the air entrapped in the bentonite buffer diffusing into the formation; once it was  
 393 saturated, large pore pressure developed due to the thermal expansion of pore water (i.e., thermal  
 394 pressurization). Hence, in general, changes in pore pressure were driven by changes in temperatures. It is  
 395 noted that the pore pressure in this study is defined as the larger between the gas and liquid pressure (  
 396  $p_{pore} = \max(p_g, p_l)$ ). Also, it was found that the timings of peak pore pressure and peak temperature did  
 397 not coincide at locations near the disposal tunnel (i.e., at V1 and H1). This is because of the poroelastic  
 398 effect playing a dominant role over the pressure diffusion; the entire rock domain around the disposal  
 399 tunnel was more or less uniformly compressed due to the thermal expansion of the formation under the  
 400 no-displacement lateral boundary condition, giving rise to spatially uniform pore pressure changes  
 401 regardless of the distance from the tunnel. This was not the case for the temperature changes as the  
 402 thermoelastic effect was negligible compared to the heat conduction. Also, there were double temperature  
 403 peaks in the near field (e.g., V1/H1, V2/H2) despite the thermal conductivity of the buffer and the  
 404 formation being constant. This is because of reverse thermal conduction from the far field to the near  
 405 field, i.e., the thermal flux bounced off the (no thermal flux) lateral boundaries and propagated back to the  
 406 near field to generate second temperature peaks.

407 Finally, although the changes in the temperature and pore pressure were more or less identical (i.e.,  
 408 symmetric) between the vertical and horizontal locations with an equal radius (e.g., V1 and H1, V2 and



409 H2, etc.), the stress changes presented in the following section were not symmetric as long as the elastic  
410 response dominated relative to the creep response. Such symmetries might be affected by the drift spacing  
411 between the disposal tunnels. In this study, the spacing of 50 m was employed as a generic scenario, but if  
412 a smaller spacing was used, for example, the temperature/pore pressure symmetry might have been  
413 distorted. The effect of different drift spacing may be examined in future studies.

414

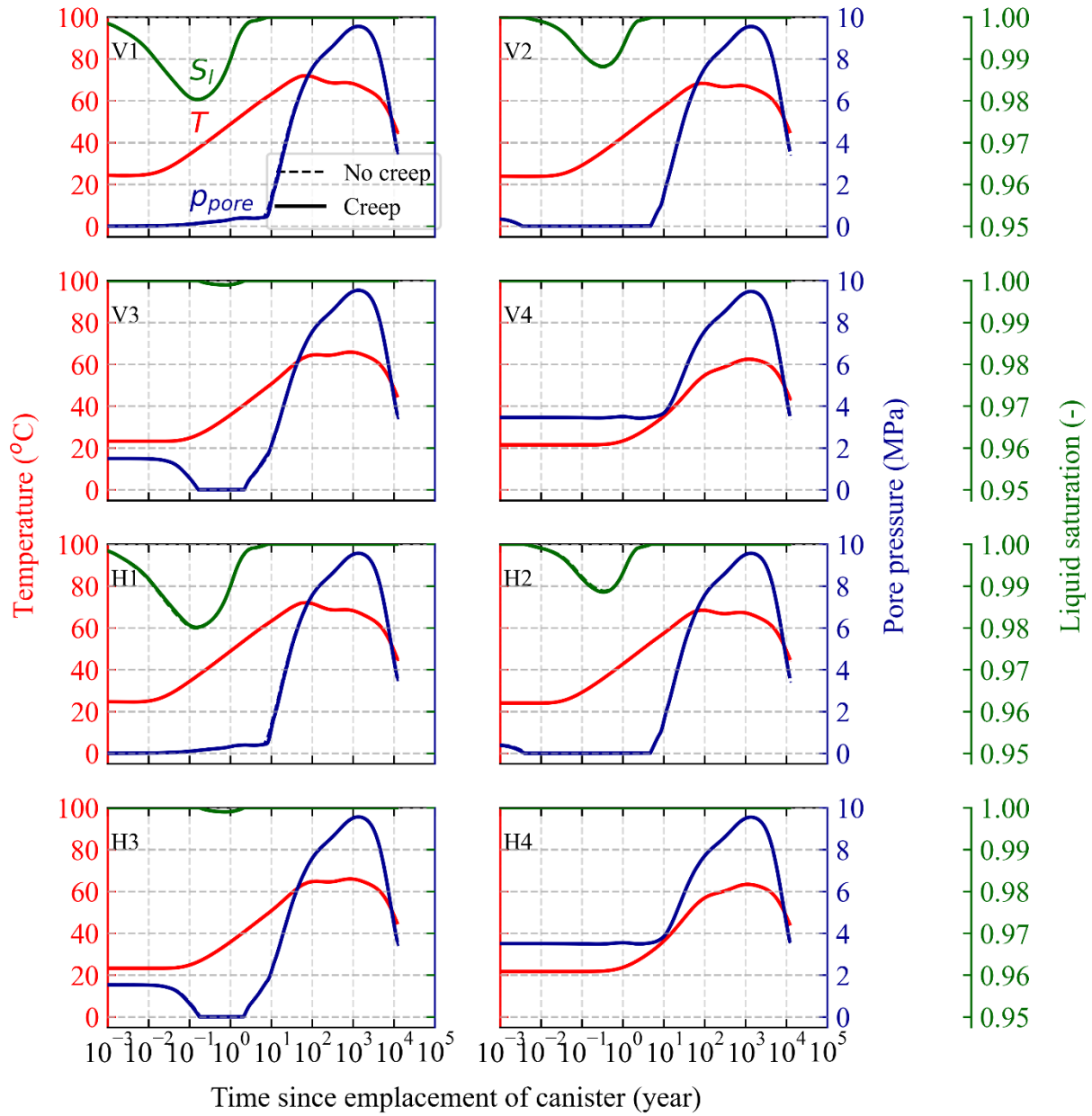


Figure 5 Changes in pore pressure, temperatures, and liquid saturation in the formation.

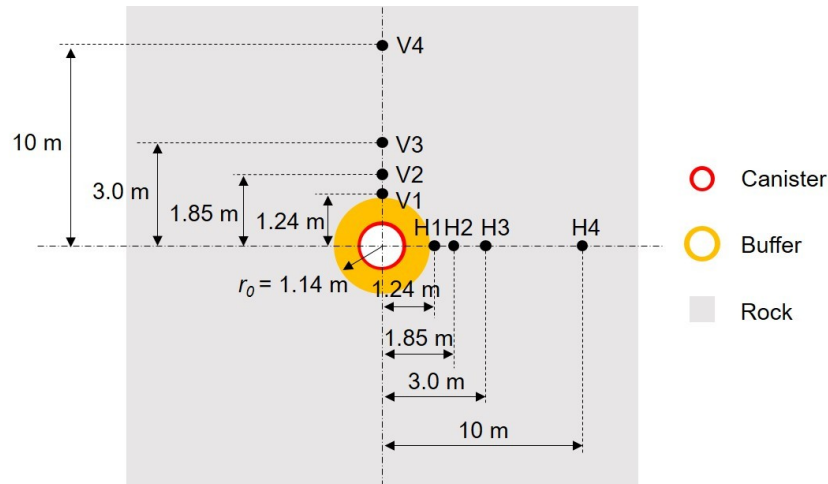
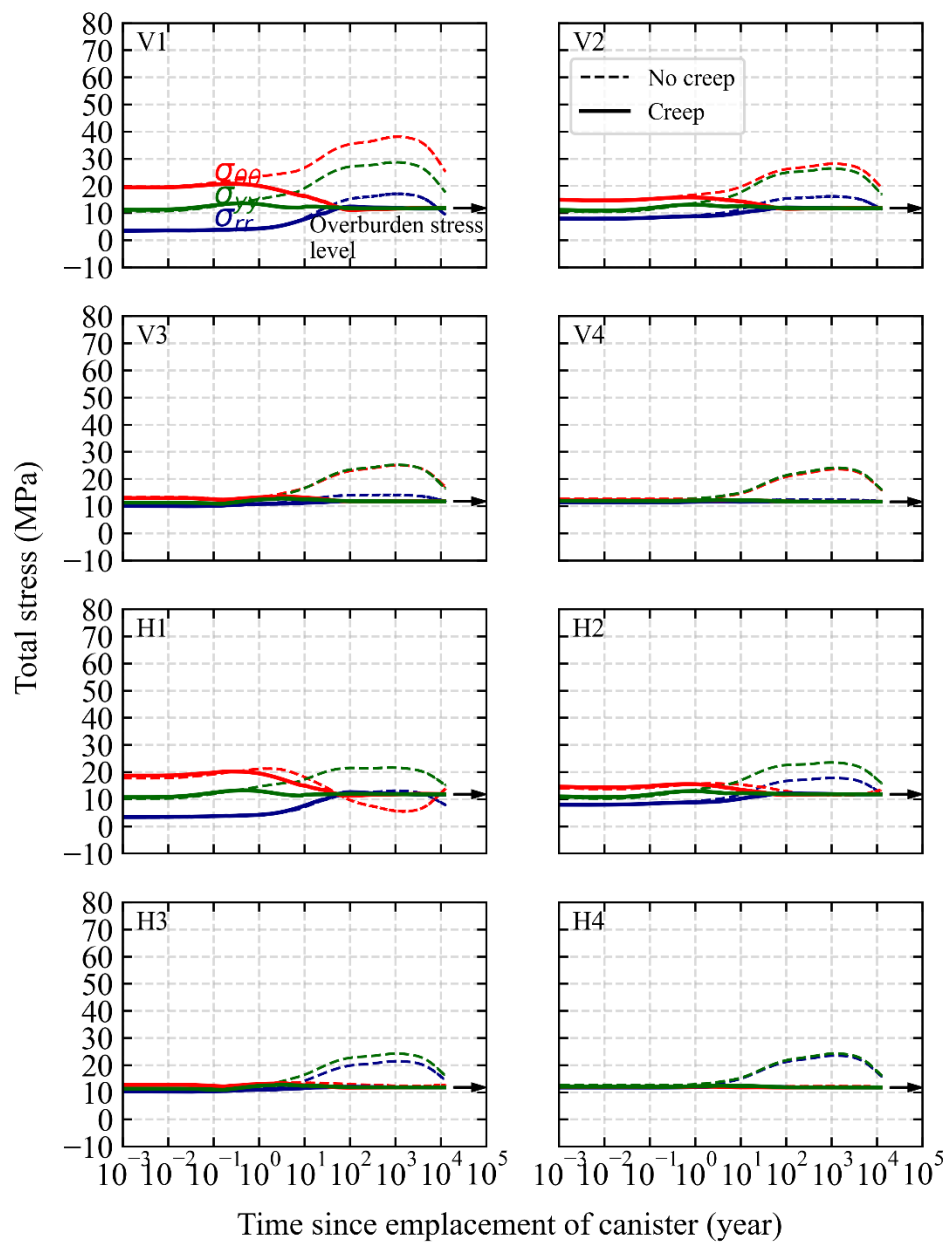


Figure 6 The locations of the data readouts in the formation <sup>12</sup>.

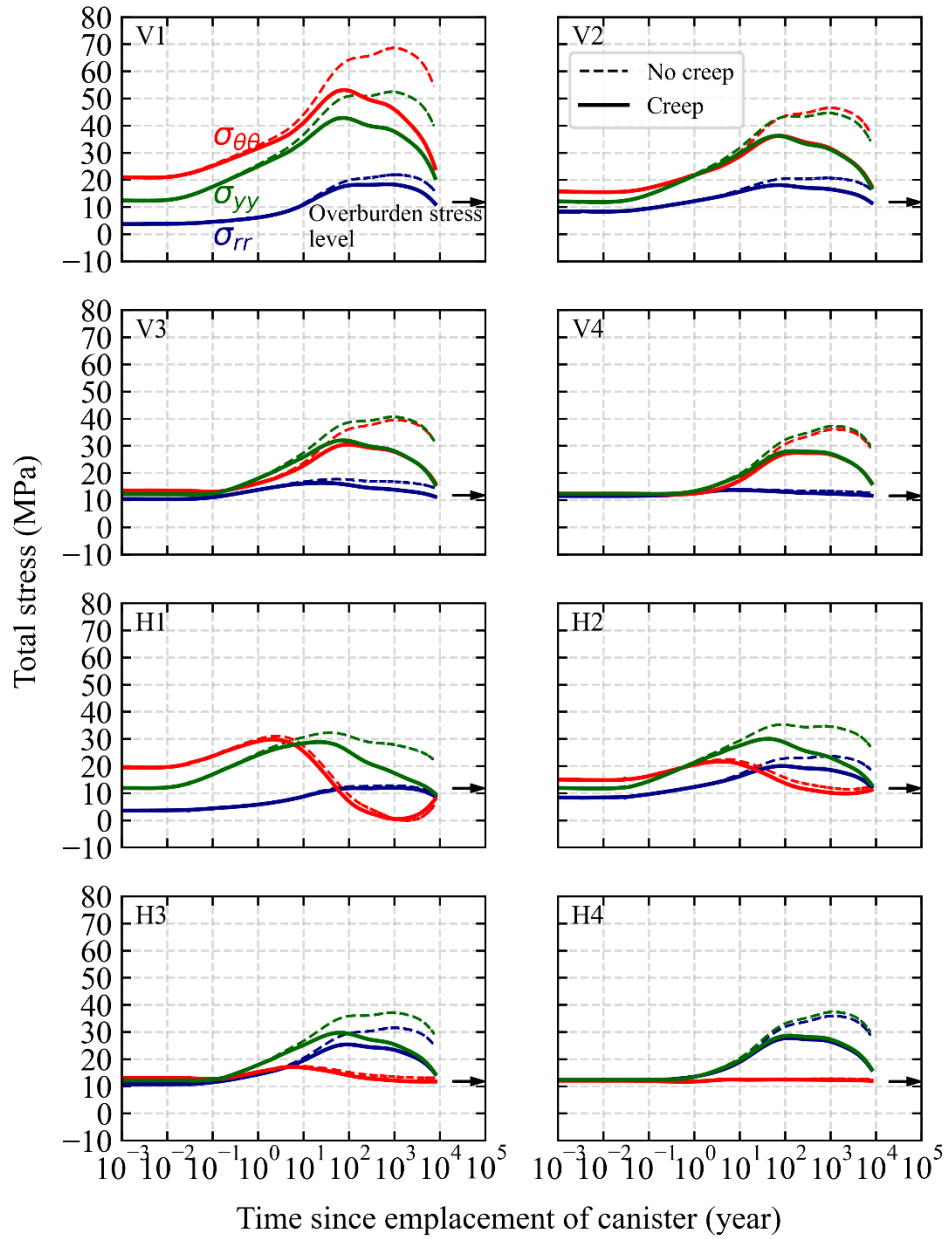
### 3.2. Stresses in the formation

Figure 7 shows changes in the total stresses in the formation. In the no creep scenarios, as well as in the creep scenario for the low creep shale case, the radial ( $\sigma_{rr}$ ), circumferential ( $\sigma_{\theta\theta}$ ), and out-of-plane ( $\sigma_{yy}$ ) total stresses increased (compression positive) at an accelerated rate from 10 years to their peak values at roughly 1,000 years at the vertical locations (i.e., V1, V2, V3, and V4), whereas at the horizontal locations (i.e., H1, H2, H3, and H4), all the stresses but the circumferential stress increased in the same manner. The decrease in the circumferential stress was caused by elliptic deformation of the tunnel; thermal expansion in the horizontal direction was constrained due to the lateral boundaries, whereas the expansion in the vertical direction was allowed because of the free surface at the top boundary, resulting in an elliptic tunnel shape with its minor (i.e., shorter) axis aligned with the horizontal axis. It is noted that this is an elasticity-dominant mechanical response in the near field; in the case where the creep response was dominant (i.e., the creep scenario for the high creep shale case), the abovementioned elliptic tunnel deformation and stress changes did not occur.

It was found that formation creep significantly decreased the stress magnitudes in both high and low creep shale cases; compared to the no creep scenarios, the circumferential, out-of-plane, and radial total stresses decreased by approximately 77%, 71%, and 35%, respectively, at 1,000 years at the V1 location in the high creep shale case, while they decreased by 33%, 27%, and 5% in the low creep shale case. The stresses approached the asymptote of 11 MPa (at the depth of 500 m), which corresponded with the isotropic geostatic stress level shown as a black arrow in Figure 7. The stress asymptotes were reached in roughly 100 years in the high creep shale case, whereas they were not reached even in 10,000 years in the low creep shale case. The slow stress decrease is due to the creep-resistant nature of the low creep shale. Also, the stiffness of such shale is usually higher than that of high creep shale. These features of low creep shale helped develop (orders of magnitude) higher stress levels in the formation for a longer period (e.g., thousands of years), which could negatively affect repository integrity. It is noted, however, that the stresses in the low creep shale case will eventually reach the same asymptote of 11 MPa if a longer period (> 10,000 years) is simulated.



(a)

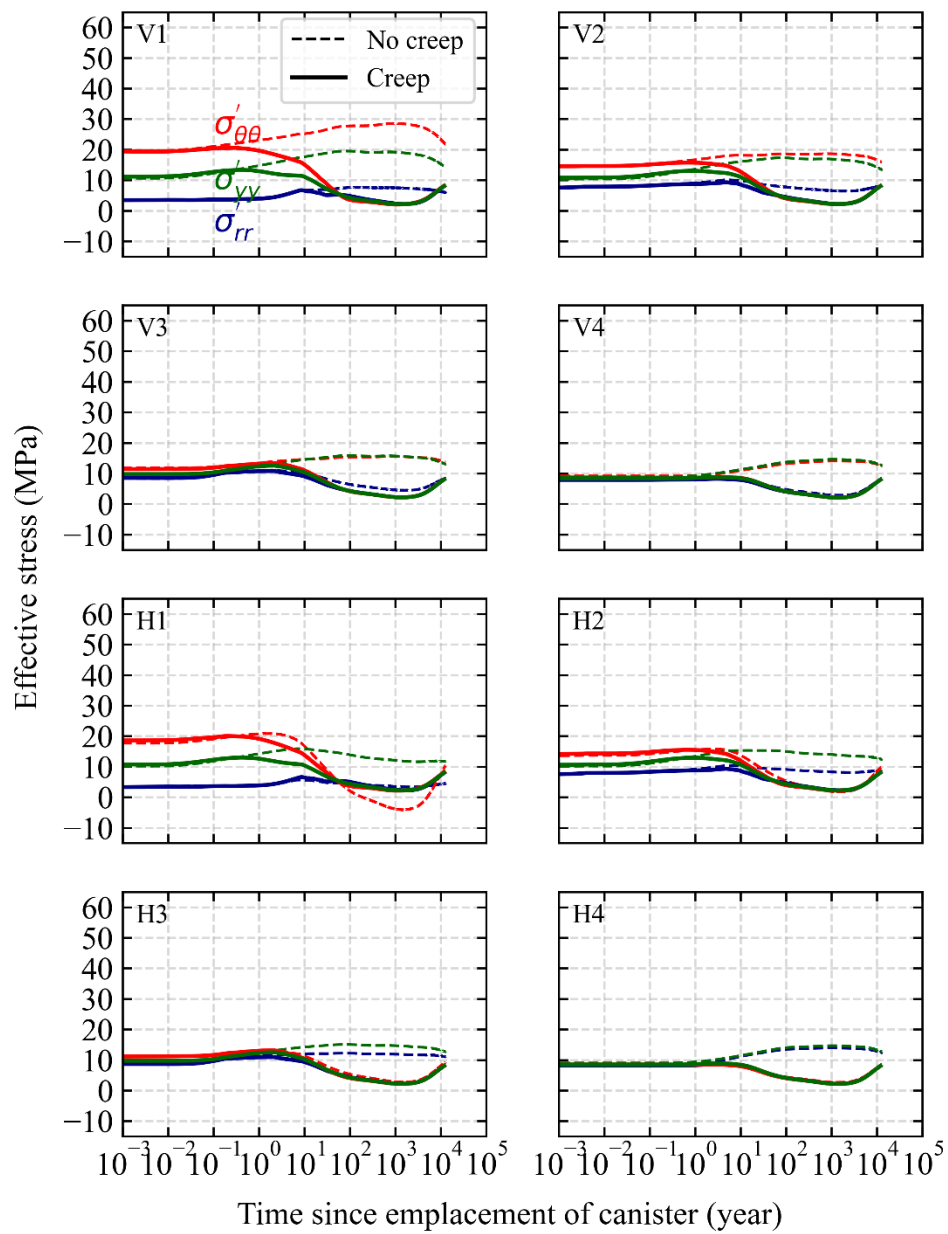


(b)

Figure 7 Changes in the total stresses in the formation: (a) high creep shale case; (b) low creep shale case.

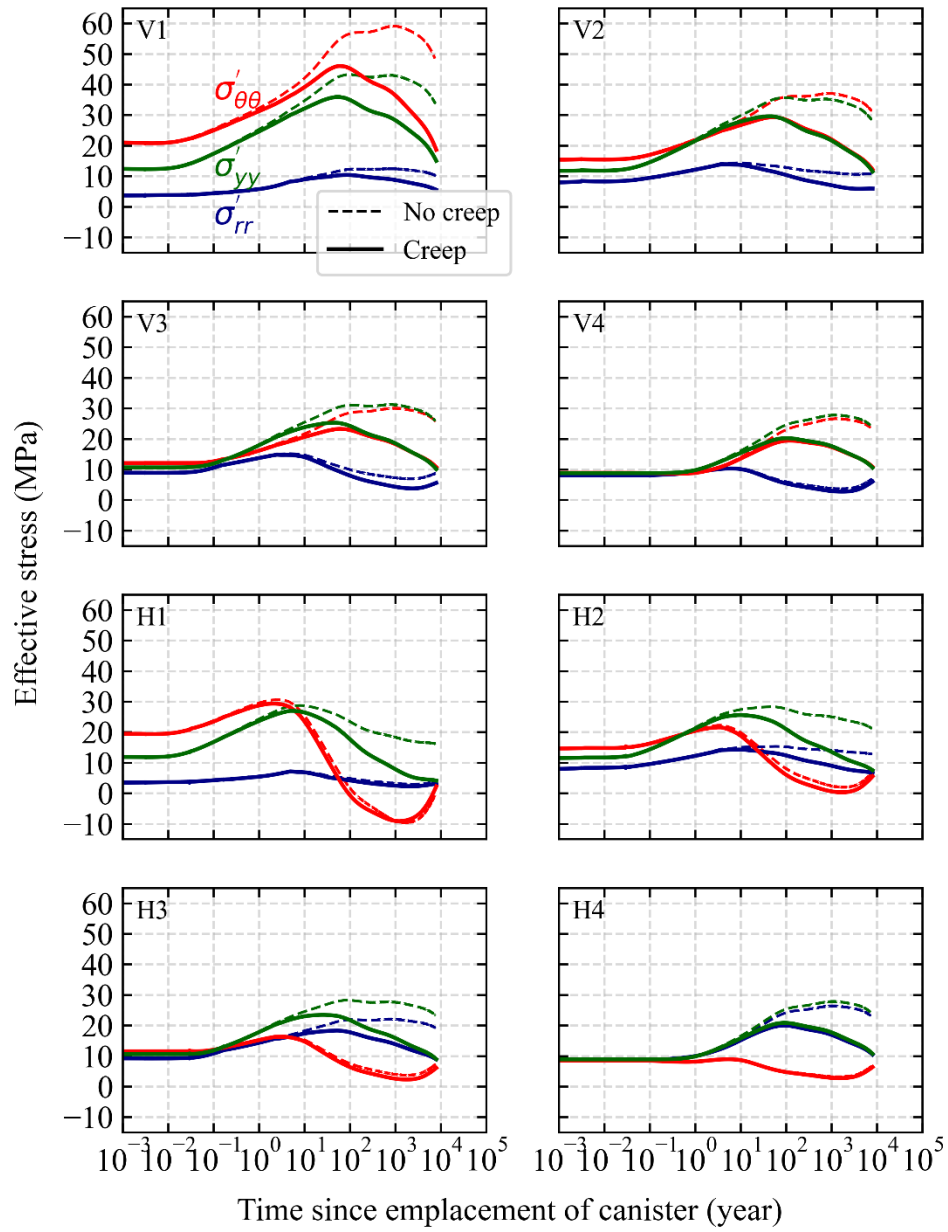
456 years due to accelerated creep, whereas in the low creep shale case, where the elasticity played a  
457 dominant role over creep in the examined timeframe (i.e., 10,000 years), the effective stresses did not  
458 become isotropic even in 10,000 years and their magnitudes were much greater than those in the high  
459 creep shale case. However, the exception was the tensile (circumferential) stresses developed at the H1  
460 location, which occurred in the low creep shale case as well as in the no creep (i.e., elastic) scenario for  
461 the high creep shale case. The maximum tensile stress levels were approximately 5 MPa and 10 MPa at  
462 roughly 1,000 years for the high (without creep) and low creep shale cases, respectively, which might be  
463 sufficient to develop fractures in the near-field formation. Hence, this further demonstrated the  
464 effectiveness of the accelerated creep in the high creep shale in enhancing (near-field) formation integrity.

465



(a)





(b)

Figure 8 Changes in the effective stresses in the formation: (a) high creep shale case; (b) low creep shale case.

Figure 9 shows changes in the mean effective ( $\sigma'_m$ ) and deviatoric ( $\sigma_d$ ) stresses. The definitions of these stresses are provided in the equations below.

$$\sigma'_m = (\sigma'_{xx} + \sigma'_{yy} + \sigma'_{zz})/3 = (\sigma'_{rr} + \sigma'_{\theta\theta} + \sigma'_{\phi\phi})/3 \quad (19)$$

$$\sigma_d = \sqrt{(1/2)[(\sigma_{xx} - \sigma_{yy})^2 + (\sigma_{yy} - \sigma_{zz})^2 + (\sigma_{zz} - \sigma_{xx})^2 + 6(\tau_{xy}^2 + \tau_{yz}^2 + \tau_{xz}^2)]} = \sqrt{(1/2)[(\sigma_{rr} - \sigma_{\theta\theta})^2 + (\sigma_{\theta\theta} - \sigma_{\phi\phi})^2 + (\sigma_{\phi\phi} - \sigma_{rr})^2 + 6(\tau_{r\theta}^2 + \tau_{\theta\phi}^2 + \tau_{r\phi}^2)]} \quad (20)$$

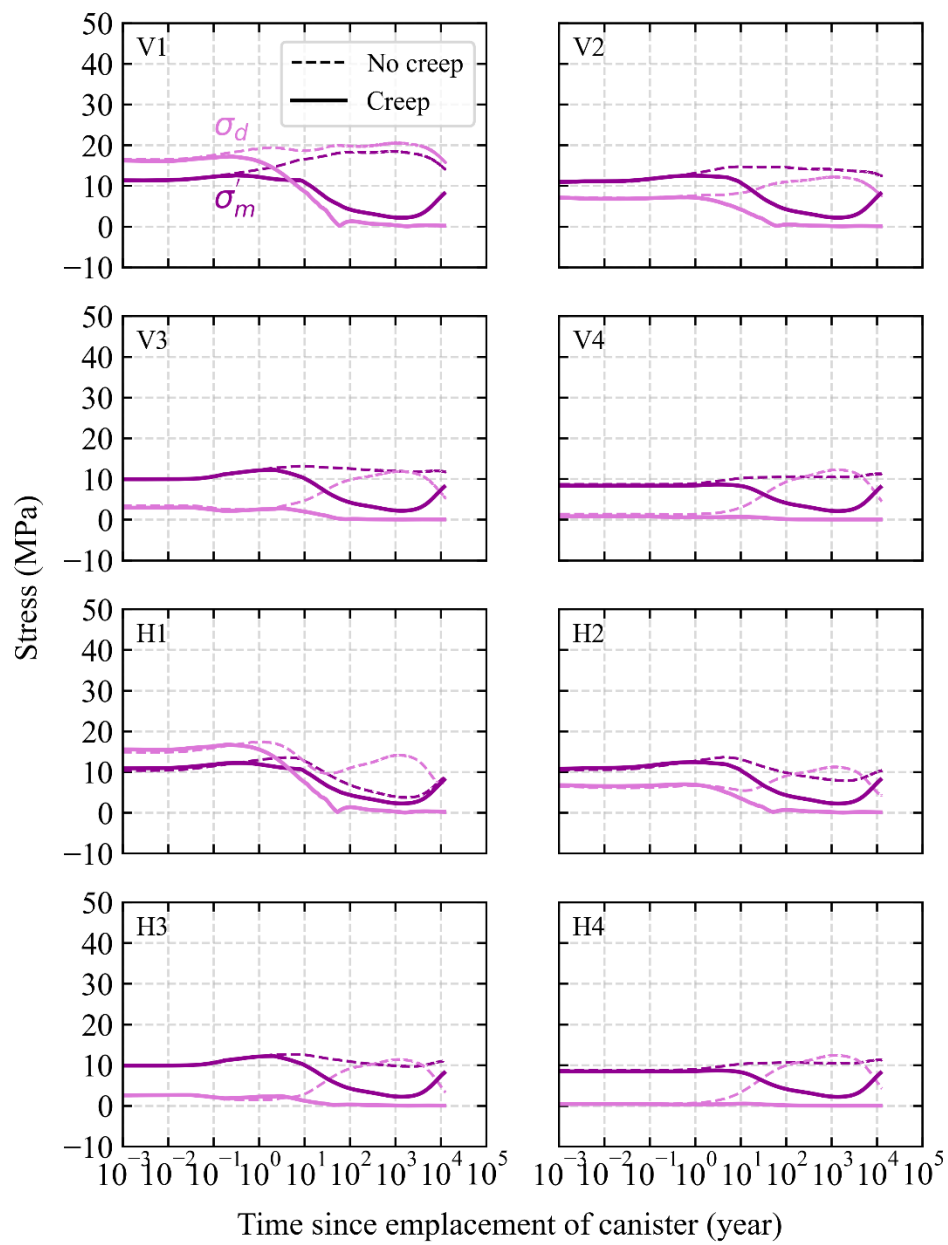
where  $\sigma'_{xx}$ ,  $\sigma'_{yy}$ ,  $\sigma'_{zz}$ ,  $\sigma'_{rr}$ ,  $\sigma'_{\theta\theta}$  are the horizontal, out-of-plane, vertical, radial, and circumferential effective stresses, respectively (the effective stress is defined as the total stress minus pore pressure ( $\sigma' = \sigma - p_{pore}$ )), while  $\tau_{xy}$ ,  $\tau_{yz}$ ,  $\tau_{xz}$ ,  $\tau_{ry}$ ,  $\tau_{y\theta}$ ,  $\tau_{r\theta}$  are shear stresses. The mean effective and deviatoric stresses are relevant to the integrity of geological nuclear waste repositories as they change formation permeability (the mean effective and deviatoric stresses, in general, cause volumetric and shear deformations of solid, respectively).

The mean effective stress levels remained more or less constant in the high creep shale case (no creep), whereas they increased significantly in the low creep shale case (no creep). This was because the cavity expansion/contraction in the near field, which was theoretically supposed to keep the mean total and effective stresses constant, was distorted (i.e., the elliptic tunnel deformation discussed earlier) due to the lateral no-displacement boundaries, which changed the mean effective stress levels in the near field, especially in the low creep shale case where they changed significantly due to its relatively high stiffness (the stiffness of the low creep shale was 2.6 times greater than that of the high creep shale). It is noted that the thermal expansion of pore water (i.e., thermal pressurization) did not affect the mean effective stress levels as it was less significant than the poroelastic pore pressure change discussed earlier in the results for the pore pressure and temperatures.

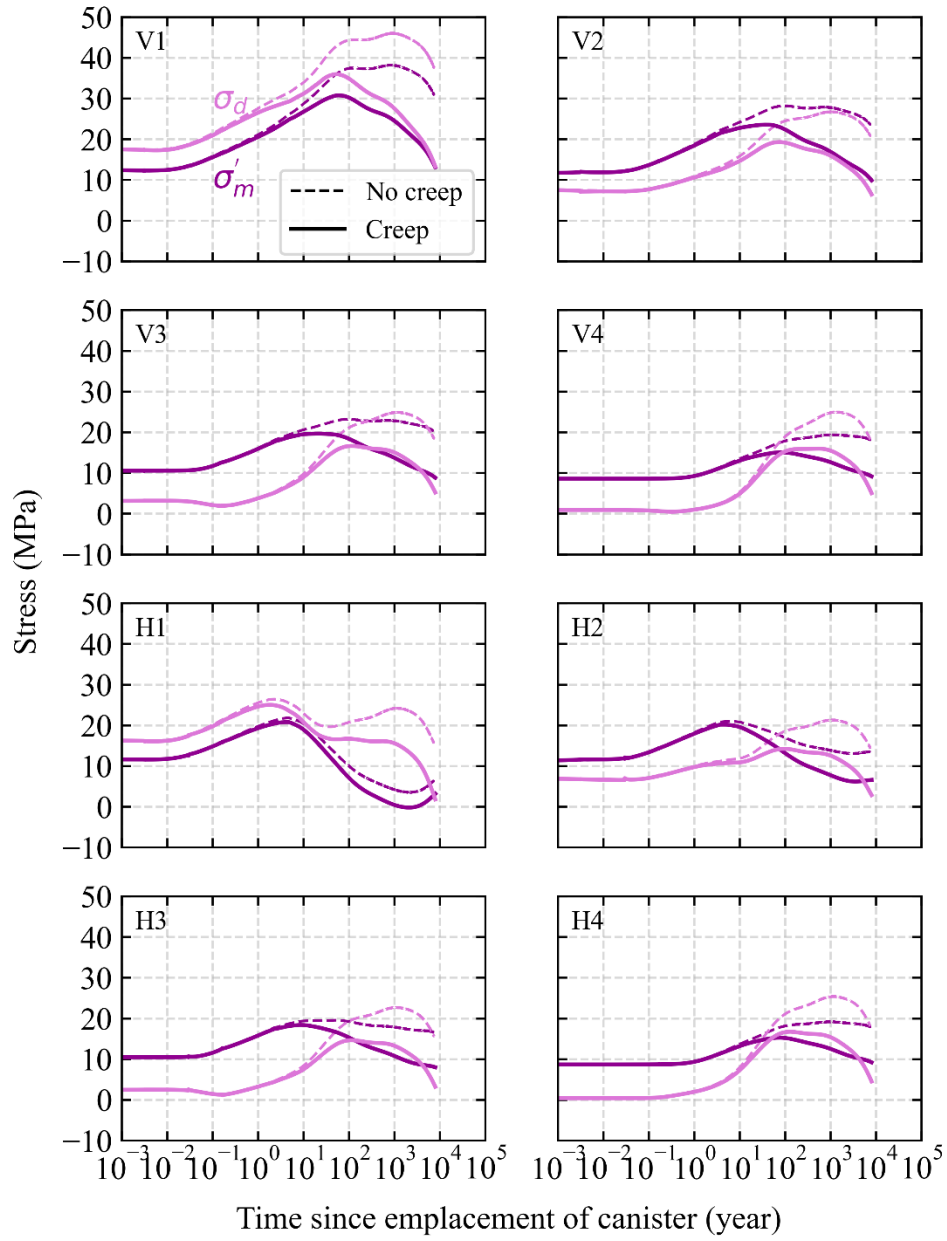
494

495 In the creep scenarios, deviatoric stress levels decreased by 100% (i.e., zero deviatoric stresses) in 100  
496 years in all examined locations in the high creep shale case, whereas in the low creep shale case, the  
497 decreases were up to roughly 50% even in 10,000 years and they were limited within the near field; in the  
498 far field (i.e.,  $V_4/H_4$ ), the deviatoric stresses even increased from the initial value of 0 MPa to roughly 5  
499 MPa. Hence, the greater the shale creep is, the less time it takes to reach the isotropic geostatic state (e.g.,  
500  $< 100$  years in the high creep shale case, whereas  $> 10,000$  years in the low creep shale case). It is  
501 emphasized that the isotropic geostatic state will eventually be recovered in the low creep shale as well if  
502 a longer period ( $> 10,000$  years) is simulated.

503 The mean effective stresses reached similar levels of roughly 10 MPa in 10,000 years in both high and  
504 low creep cases at all locations (except for the H1 location for the low creep shale case where the tensile  
505 stress developed as discussed earlier). However, the mean effective stress levels were as small as roughly  
506 1 MPa at 1,000 years in the high creep shale case, whereas they were as large as 30 MPa at 100 years in  
507 the low creep shale case. The former was due to creep-induced stress relaxation combined with pore  
508 pressure increase, while the latter was because of elasticity-induced thermal stress development. This  
509 shows that the mean effective stress levels in the formation could temporarily decrease to one tenth of the  
510 initial levels at around 1,000 years due to accelerated creep, which is detrimental to the formation  
511 integrity (e.g., increases in fracture permeability, decreases in shear strength, etc.).



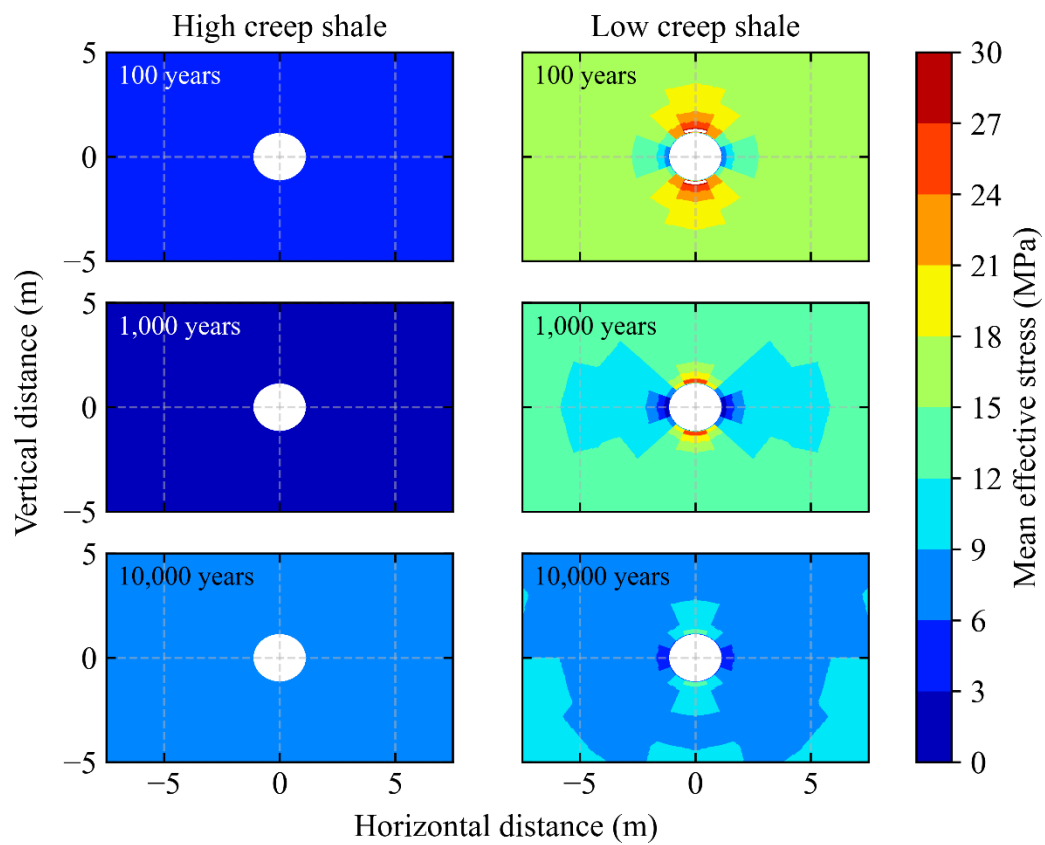
(a)



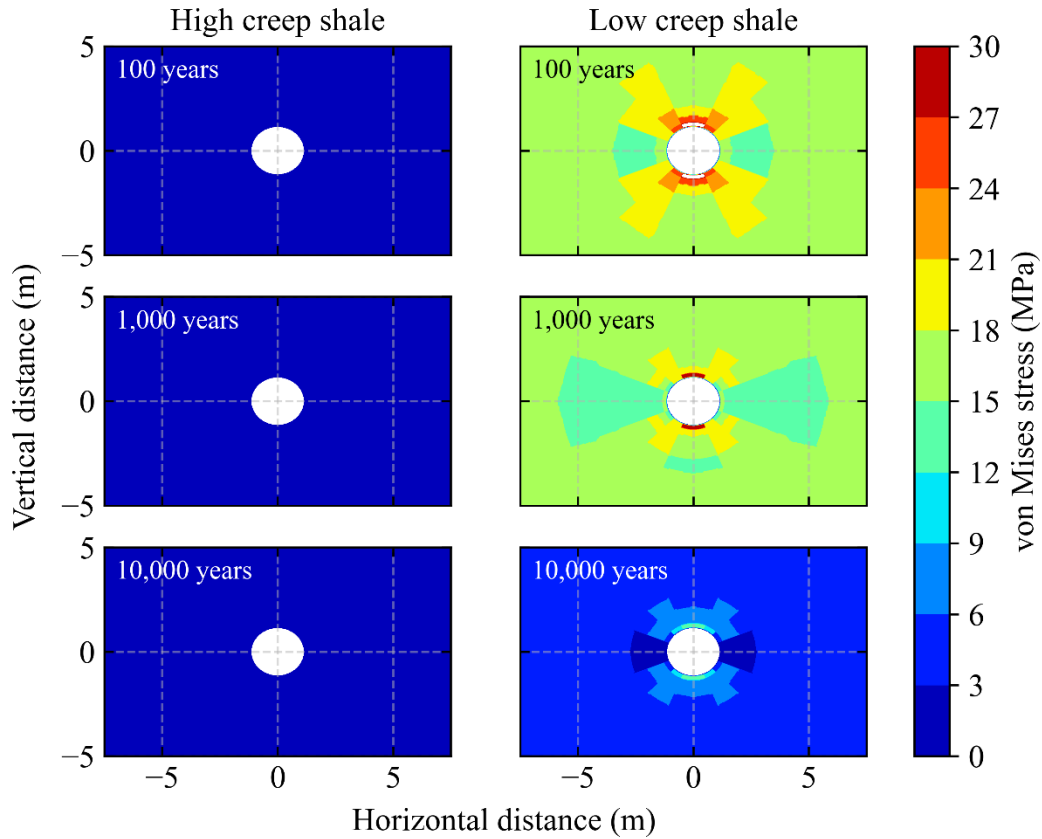
(b)

Figure 9 Changes in the mean effective and deviatoric stresses in the formation: (a) high creep shale case; (b) low creep shale case.

Figure 10 shows stress contours around the disposal tunnel comparing the stress evolution between the high and low creep shale cases (with creep). In the low creep shale case, both the mean effective stress (Figure 10a) and the deviatoric stress (Figure 10b) concentrated around the tunnel (e.g., 50-100% greater stress magnitudes in the near field (e.g., radius  $\approx 1$  m) than in the far field (e.g., radius  $> 5$  m) at 100 years), whereas in the high creep shale case, the stress levels were uniform, isotropic and less than those in the low creep shale case. The uniform and decreased stress levels are due to accelerated creep as well as the relatively low stiffness of the high creep shale. The decreased stress levels, however, does not necessarily indicate better formation integrity as decreases in the mean effective stress could allow fractures to open, which increases the formation permeability. Decreases in the deviatoric stress, on the other hand, lower the chance of generating fractures and thereby reduce the formation permeability. These competing effects of decreased stress levels due to creep on the formation permeability are discussed in the following section.



(a)



(b)

Figure 10 Contour plots comparing stress profiles around the disposal tunnel between the high and low creep shale cases; (a) mean effective stress; (b) deviatoric stress (i.e., von Mises stress).

### 3.3. Formation permeability

Figure 11 shows changes in permeability in the formation. As mentioned in the previous section, permeability values are estimated from the deviatoric and mean effective stresses, and it is calculated from an empirical equation shown below <sup>50</sup>.



$$k = \left( k_r + \Delta k_{max} \exp(\beta_1 \sigma'_m) \right) \cdot \exp(\gamma \langle \sigma_d - \sigma_{d,crit} \rangle) \quad (21)$$

where  $k_r$  is the residual permeability,  $\Delta k_{max}$  is the maximum permeability increment at zero mean effective stress,  $\beta_1$  is a mean effective stress parameter,  $\sigma'_m$  is the mean effective stress,  $\gamma$  is a deviatoric stress parameter,  $\sigma_d$  is the deviatoric stress, and  $\sigma_{d,crit}$  is the critical deviatoric stress magnitude. Note that  $\langle \rangle$  signifies the MaCaulay brackets; if the value inside the brackets is negative, it returns zero, whereas if the value is positive, it returns the unmodified value. The above equation (Eq. (21)) was applied to the formation within the radius of 3.6 m from the center of the disposal tunnel, which is roughly three times the radius of the tunnel, while a constant permeability value of  $k_r$  was applied in the rest of the formation domain. The values of the parameters of the permeability function are listed in Table 4. These parameters were also developed and applied in the previous work <sup>12</sup>, where it was shown that the function (Eq. (21)) could model permeability increases of several orders of magnitude in the excavation disturbed zone around a tunnel, which are comparable with what has been observed at underground research laboratories in shale <sup>8,51</sup>. Such permeability increases near the tunnel are explained by Eq. (21) as increases in the deviatoric stress due to cavity contraction, which is evident in Figure 9 at  $t = 0$  where the mean effective stress levels were nearly identical at the geostatic level of roughly 11 MPa at different horizontal locations, whereas the deviatoric stresses increased with decreasing distance from the tunnel. The post-excavation permeability increase can be seen at the V1 and H1 locations at  $t = 0$  (i.e.,  $\sim 1 \cdot 10^{-18} \text{ m}^2$  (post-excavation) vs.  $5 \cdot 10^{-20} \text{ m}^2$  (intact, pre-excavation)) (Figure 11a and b).

Table 4 The values of the parameters of the empirical permeability function.

Residual permeability, $k_r$ ( $\text{m}^2$ )	$5 \cdot 10^{-20}$
---	--------------------

Permeability increment, $\Delta k_{max}$ (m <sup>2</sup> )	$1 \cdot 10^{-17}$
Mean effective stress parameter, $\beta_I$ (1/Pa)	$-1 \cdot 10^{-6}$
Deviatoric stress parameter, $\gamma$ (1/Pa)	$3 \cdot 10^{-7}$
Critical deviatoric stress, $\sigma_{d, crit}$ (Pa)	$5 \cdot 10^6$

---

565

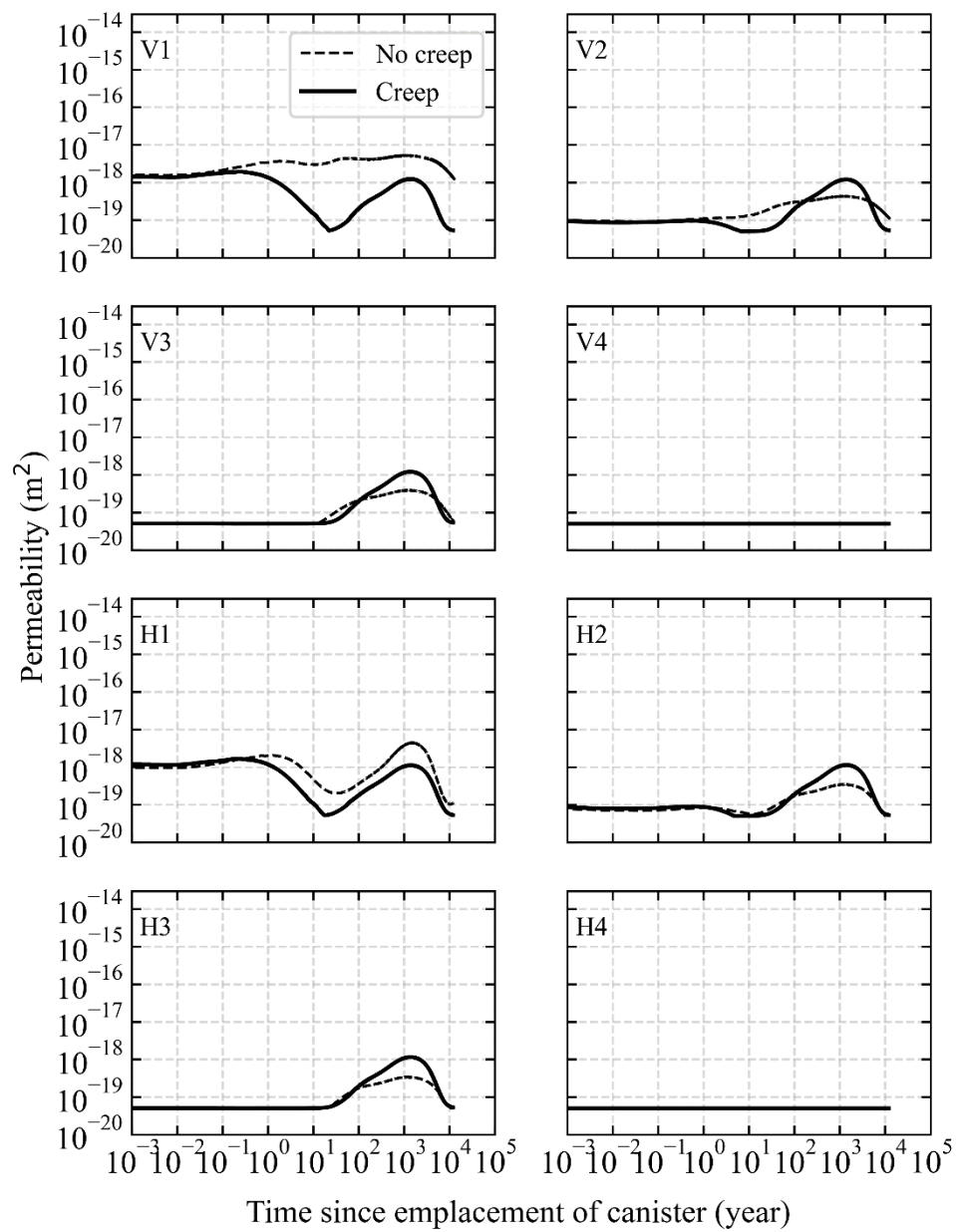
566 In the high creep shale case with no creep, permeability increased by approximately two orders of  
567 magnitude from the baseline value of  $5 \cdot 10^{-20}$  m<sup>2</sup> at 1,000 years at the V1 and H1 locations (Figure 11a).  
568 The permeability increased as the deviatoric stress increased and/or the mean effective stress decreased,  
569 both of which increase permeability as shown in Eq. (21). A drastic permeability increase of five orders of  
570 magnitude was calculated in the low creep shale case at 1,000 years at the V1 location, as the deviatoric  
571 stress increased by more than 100% from its initial value at this location. It is noted that whether these  
572 absolute permeability estimates are accurate or not is not the scope of this study; it is the comparison  
573 between the creep and no creep scenarios that matters as it reveals the effect of creep on formation  
574 integrity. The abovementioned trends in the no creep scenarios are used as baselines to assess the effect of  
575 creep.

576

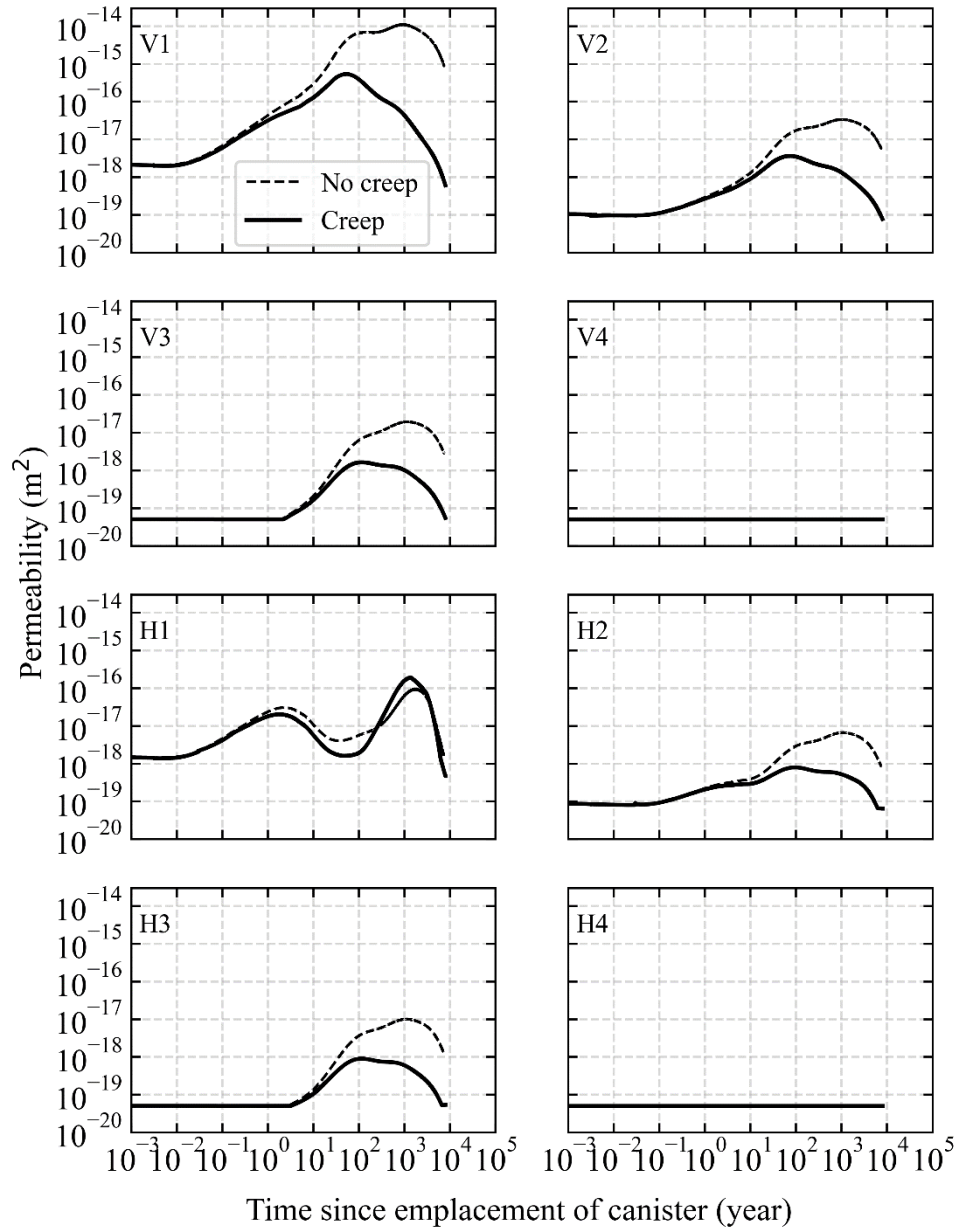
577 Compared to the baseline, no creep scenarios, results from the creep scenarios show lower permeability  
578 values, e.g., as much as three orders of magnitude lower in the low creep shale case at V1 location at  
579 10,000 years. This is attributable to significant decreases in the deviatoric stress (50% to 100% decrease  
580 compared to the no creep scenarios) over the long term due to shale creep. In some locations in the high  
581 creep shale case (e.g., V2, V3, H2, H3), however, permeability values in the creep scenario temporarily  
582 surpassed those in the no creep scenario at around 1,000 years. This is due to creep-induced isotropic and  
583 constant total stress condition (i.e., isotropic geostatic state), which decreased the effective stresses when  
584 the pore pressure increased to its peak values at roughly 1,000 years. The creep-induced isotropic and

585 constant total stress condition occurred as the Norton-Bailey law is a deviatoric creep law where the  
586 deviatoric stress, which is independent of pore pressure, is the driver of creep strains; since the only  
587 constant stress in the formation was the vertical total stress in the far field (i.e., overburden stress), the  
588 deviatoric creep law worked to adjust the lateral effective stresses by generating creep strains until they  
589 were in equilibrium with the vertical effective stress (i.e., zero deviatoric stress). As the sum of the  
590 vertical effective stress and pore pressure was always constant at the overburden stress (in the far field),  
591 the lateral total stresses also became equal to the overburden stress, and hence the isotropic geostatic state  
592 was recovered. This equilibrium propagated from the far field, where the effect of distorted cavity  
593 contraction/expansion was minimal, to the near field.

594 These results suggest that the formation integrity could improve with increasing creep in the long term  
595 (~10,000 years) but not in the intermediate term (~1,000 years). It is noted, however, that the effect of  
596 creep (or that of tensile fracturing) is not incorporated into the employed permeability function. The effect  
597 of creep would be such that the permeability does not increase during creep-induced mean effective stress  
598 relaxation due to simultaneous creep-induced irrecoverable fracture closure. Thus, the permeability  
599 should not be a function of only the changes in the mean effective stress but it should also be a function of  
600 creep-related variables. Note that the effect of deviatoric stress on the permeability function should still be  
601 valid as decreases in the deviatoric stress decrease the chances of shear-induced fracture dilation, new  
602 fracture development, etc. The development of a new permeability function that can take the creep effect  
603 into account may be addressed in future studies.



(a)



(b)

Figure 11 Changes in permeability in the formation: (a) high creep shale case; (b) low creep shale case.

Figure 12 shows permeability contours around the disposal tunnel comparing the permeability evolution between the high and low creep shale cases (with creep). As expected, significantly greater permeability

612 values were developed in the low creep shale case than in the high creep shale case (e.g.,  $\sim 10^{-16} \text{ m}^2$  vs.  
613  $\sim 10^{-19} \text{ m}^2$  at 100 years near the tunnel), which is due to greater deviatoric stress levels in the low creep  
614 shale case. At 1,000 years, however, the permeability levels in the high creep shale case increased to  
615 similar values developed in the low creep shale case (i.e.,  $\sim 10^{-18} \text{ m}^2$ ). This is because, in the high creep  
616 shale case, mean effective stress levels decreased while deviatoric stress levels remained at zero (i.e., net  
617 increases in permeability) in the near field between 100 and 1,000 years, whereas in the low creep shale  
618 case, greater mean effective stress levels (than those in the high creep shale case) overcompensated for the  
619 increased deviatoric stress levels (i.e., net decreases in permeability). The permeability levels in both  
620 shale cases tend to decrease in 10,000 years to the value of intact bedrock (i.e.,  $5 \cdot 10^{-20} \text{ m}^2$ ), but the  
621 decrease was slower in the low creep shale case. Thus, it was found that high creep shale could achieve  
622 better formation integrity than low creep shale in the short (100 years) and long (10,000 years) terms,  
623 while in the intermediate term (1,000 years), creep properties of shale might not significantly affect the  
624 formation integrity.

625

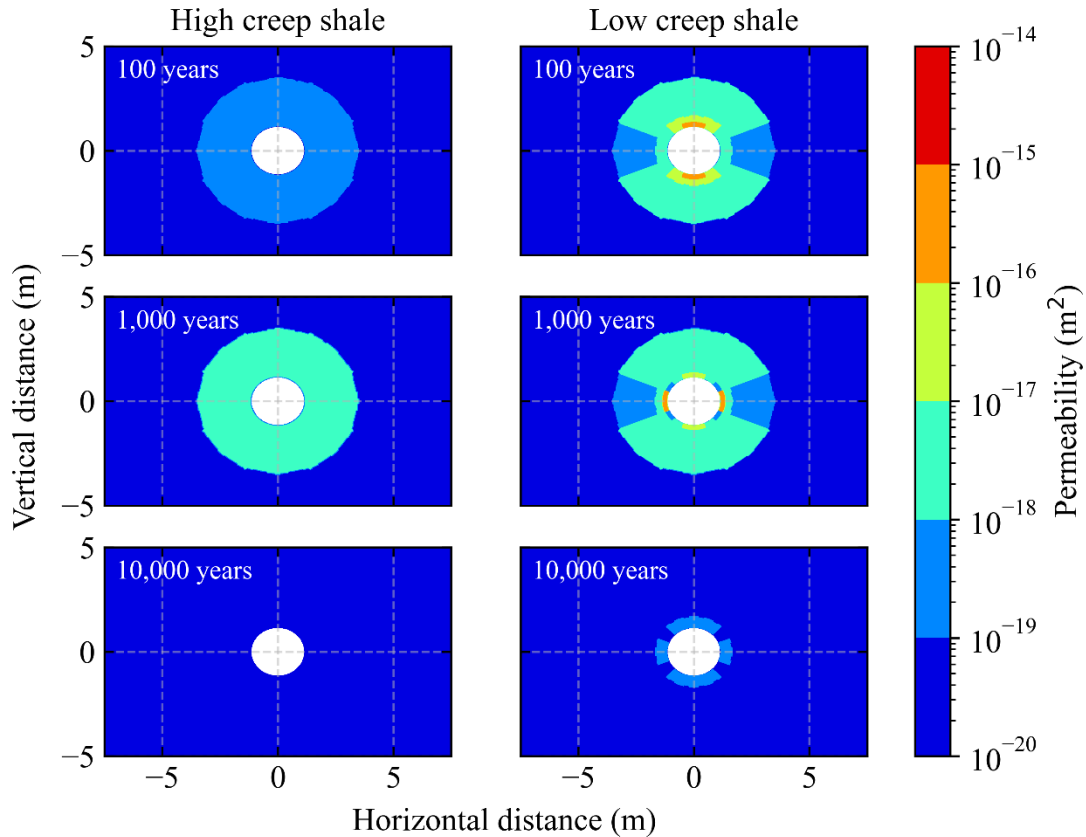


Figure 12 Contour plots comparing permeability profiles around the disposal tunnel between the high and low creep shale cases.

### 3.4. Pressure, temperatures, and stresses in the bentonite buffer

As the scope of this study is to investigate the effect of formation creep on long-term integrity of the repository, not only the integrity of the formation but also that of the bentonite buffer is of great importance as the buffer is engineered to be a barrier against potential radionuclide release. The swelling of the buffer tightens the buffer itself and also seals any cavity or fractures that may develop in the excavation disturbed zone. In other words, the swelling of the buffer provides the tunnel with confining stress and thereby decreases deviatoric stresses in the excavation disturbed zone in addition to increasing

the mean effective stress in the buffer itself. However, creep-induced tunnel deformations may impact the stress development in the swelling buffer. Therefore, the interaction between the buffer and the surrounding host rock with different creep properties are examined herein.

Figure 13 shows changes in TH outputs in the buffer, which were evaluated at the middle thickness of the bentonite buffer (i.e.,  $r \cong (OD_B + ID_B)/4$  ( $OD_B$  and  $ID_B$  are the outer and inner diameters of the bentonite buffer, respectively)) in the upper vertical direction ( $\theta \cong 90^\circ$  from the positive x-axis in the counterclockwise direction). Differences between the creep and no creep scenarios were found negligible (i.e., the solid and dashed lines representing each scenario overlap each other), and so were differences between the high and low creep shale cases. Hence, only the results for the high creep shale case is provided. Changes in the buffer pore pressure and temperatures followed those of the formation; the peak temperature of approximately 80°C developed at slightly before 100 years, whereas the peak pore pressure of about 10 MPa developed at roughly 1,000 years. The delay in the peak pore pressure relative to the peak temperature is caused by the thermal pressurization in the surrounding formation (i.e., slow thermal transport vs. fast pore pressure propagation from the surrounding formation to the buffer). It is noted that the pore pressure in the buffer was initially close to zero because it was not fully saturated until 10 years. As the buffer became saturated, the swelling of the bentonite buffer developed.



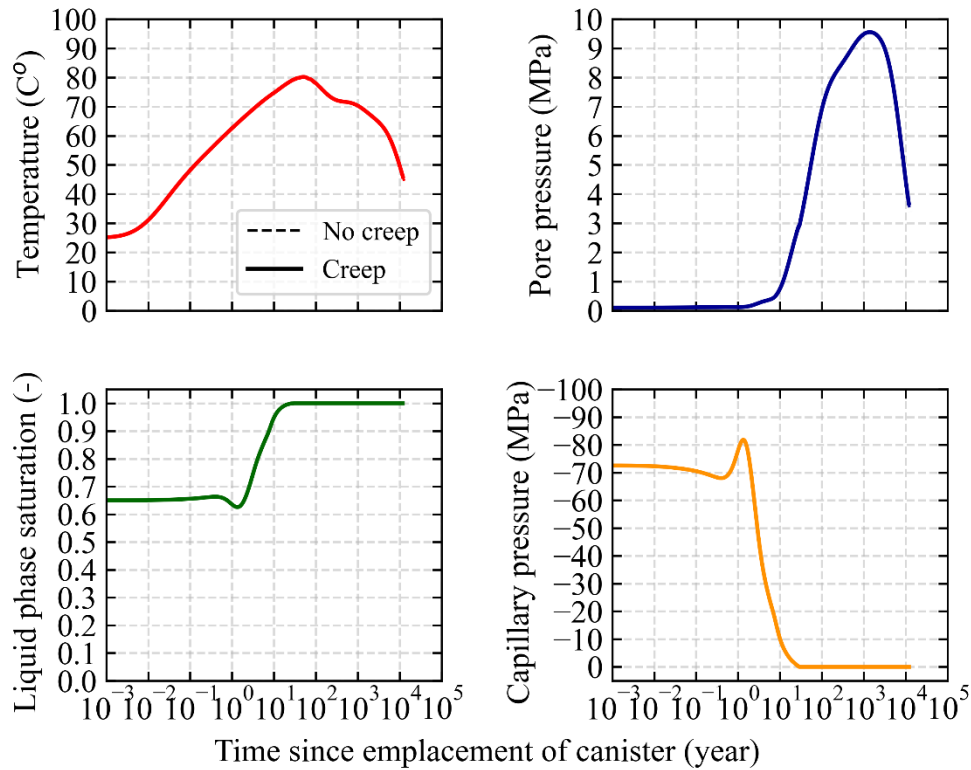
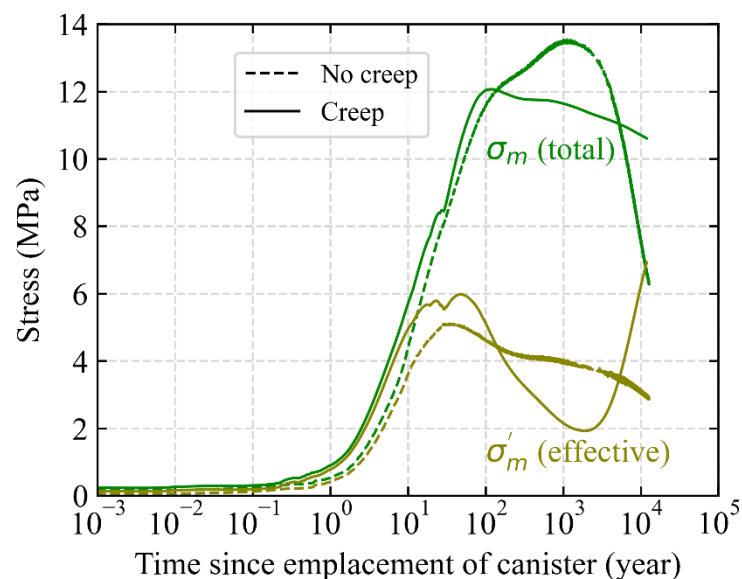


Figure 13 Changes in temperature, pore pressure, liquid phase saturation, and capillary pressure in the bentonite buffer.

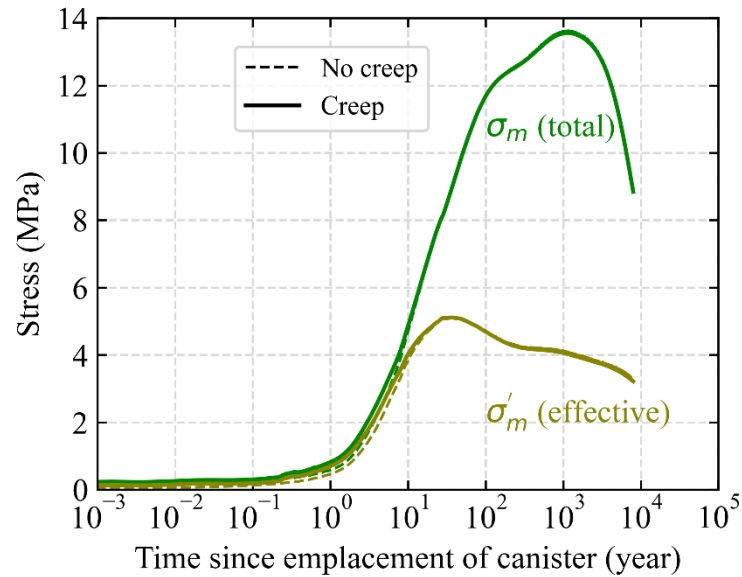
Figure 14 shows changes in the mean total and effective stresses in the buffer. The increases in these stresses between approximately 1 year and 30 years are due to saturation-induced buffer swelling, whereas the increases between 30 years and approximately 100 years are due to the thermal expansion of the buffer. The subsequent stress changes after 100 years are due to changes in pore pressure as well as deformations of the disposal tunnel. For example, the timing of the peak total stress matches the timing of peak pore pressure (i.e., ~1,000 years) (no creep scenario). The total stress in the high creep shale case, however, does not have a corresponding peak at ~1,000 years (creep scenario) (Figure 14a). This is because of the formation creep; the total stress in the buffer could not increase above the geostatic stress level of the formation (i.e., ~11 MPa) in the high creep shale case. Meanwhile, the formation creep also

caused the radius of the disposal tunnel to decrease by approximately 2 cm between 1,000 and 10,000 years. This creep-induced tunnel shrinkage helped maintain the geostatic stress level exerted on the bentonite buffer even after the pore pressure and temperatures decreased from 1,000 years. This led to a significant increase in the mean effective stress from 2 MPa at 1,000 years to nearly 7 MPa at 10,000 years (i.e., solid light green curve in Figure 14a). This increase in the effective stress in the buffer is beneficial to the repository integrity as it will not only densify the buffer itself but also help close any opening between the buffer and rock, thereby decreasing the permeability of the whole system around nuclear waste canisters. It is noted, however, that the mean effective stress temporarily decreased to just 2 MPa at 1,000 years, which was about half the effective stress developed in the low creep shale case (and in no creep case). This is again due to the creep-induced total stress plateau in the high creep shale case. Hence, there seems to be a tradeoff between the intermediate-term (~1,000 years) and long-term (~10,000 years) bentonite buffer integrity depending on the creep characteristic of the surrounding formation; repository integrity increases with increasing creep in shale (i.e., high creep shale) in the long-term, although in the intermediate term, it may become better with less in creep in shale (i.e., low creep shale).



684

(a)



685

686

(b)

687 Figure 14 Changes in the mean total and effective stresses in the buffer: (a) high creep shale case; (b) low  
 688 creep shale case.

689

## 690 4. Discussion

691 The present study focuses on long-term (~10,000 years), time-dependent deformation of shale and their  
 692 effects on stress and permeability changes in a geological nuclear waste repository. To the best of our  
 693 knowledge, this study is first-of-its-kind in terms of applying shale creep to the long-term performance  
 694 assessment of a geological nuclear waste repository. Previous studies on the modeling of long-term THM  
 695 coupled behaviors of geological nuclear waste repositories in clayey rocks (e.g., clay, argillite, shale, etc.)  
 696 <sup>13,14</sup> did not consider the effect of formation creep as the host rock was assumed completely elastic. Effects  
 697 of creep were included in the modeling of nuclear waste repositories in salt formations, including damage,

sealing and healing<sup>15-17</sup>. Their buffer material was crushed salt and the host rock was salt, which differed from the system examined in this study (i.e., the buffer material was bentonite and the formation was shale). Thus, the findings of this research, such as reduced formation permeability and increased buffer effective stress in the long term, are unique to shale repositories in the literature.

It is important, however, to examine the model assumptions to bolster the credibility of the findings. First, the use of the power-law creep model to simulate long-term, time-dependent deformations of the formation is valid because the computed maximum deviatoric stress levels ( $< 50$  MPa) and temperatures ( $< 80^{\circ}\text{C}$ ) are both relatively low, suggesting that the formation would exhibit only the primary creep. In fact, studies show that under such stress and temperature conditions, shales exhibited only the primary creep behaviors in laboratory experiments<sup>21-23</sup>. In addition, their experimental results also validated the assumption that the value of the  $n$  exponent is equal to unity for shales under the condition that the deviatoric stress level is relatively low (i.e.,  $< 80$  MPa). The choice of the Norton-Bailey model among other power-law creep models is sensible as the Norton-Bailey model is applicable under intermediate to low deviatoric stress levels ( $< 60$  MPa), whereas more traditional power-law models could only work under higher deviatoric stress levels ( $< 200$  MPa)<sup>24</sup>.

Second, it was assumed that the  $A$  parameter of the Norton-Bailey creep model is temperature-dependent but not confining stress-dependent. The other parameters (i.e., exponents,  $m$ , and  $n$ ) were also assumed to be neither temperature- nor stress-dependent. These assumptions have been validated by laboratory experiments on clay- and/or organic-rich shales<sup>24,31</sup>. For carbonate-rich shale, however, the  $m$  exponent might become stress- and temperature-dependent<sup>23</sup>.

Third, the volumetric creep (i.e., creep due to changes in the mean effective stress) was ignored in this study. This assumption has been experimentally validated for different shales with only few exceptions (e.g., Haynesville-Dark shale)<sup>20,21,36</sup>. Volumetric creep in combination with deviatoric creep can be modelled with more advanced creep models<sup>52,53</sup>, but this is out of scope of this study.

Fourth, a deviatoric stress threshold, under which creep would not occur, was not considered in this study. This seems valid for shales as laboratory experiments show that such threshold was not clearly observed in shales<sup>21</sup>, although there might be such a threshold in argillaceous rocks<sup>54</sup>.

It is noted that some creep mechanisms are not included in the above discussion, such as creep due to rock grain-pore fluid interaction<sup>55–57</sup>, as such creep mechanism is not explicitly modeled in this study.

Finally, the function that was used to evaluate permeability changes (Eq. (21)) is simple but capable of quantifying the impact of high and low creep shales on the permeability evolution. For example, in the high creep shale case (i.e., high clay content), Eq. (21) decreases the permeability with decreasing deviatoric stress due to creep. However, it is likely that the current permeability model does not fully account for creep- and internal swelling-induced fracture closure in shale with higher clay content<sup>58</sup>. Thus, improved permeability models need to be developed from laboratory and field tests dedicated for examining long-term fracture sealing<sup>18,58</sup>.

Also, as the sealing capability of shales and clays can be characterized by their clay contents, it is important to examine the clay contents of the modeled Caney shale against those of other shales/clays, in

order to put the creep properties of the high and low creep (Caney) shales into perspective. Figure 15 shows the clay content (+ total organic content (TOC)) and other mineral compositions (carbonate, and quartz + feldspar + pyrite (QFP) contents) of different shales and clays<sup>19,21,34,59</sup>. Figure 15 categorizes the shales and clays into either 'sealing' or 'brittle' by the dashed line representing the threshold clay content (+ TOC) of roughly 33%<sup>60</sup>. According to the figure, the high and low creep (Caney) shales (shown by the 'x' symbols) qualify as 'sealing' and 'brittle', respectively. Hence, the perspective of clay content validates the use of Caney shale as both high and low creep shales. It is noted, however, that some shales could be more creep-prone (e.g., Pierre shale) or creep-resistant (e.g., Barnett shale) than Caney shale, as their clay contents are significantly greater and less than those of Caney shale, respectively. More experimental data for these (and other) shales on their creep properties are necessary to assess their creep-induced sealing behaviors in geological nuclear waste repositories.

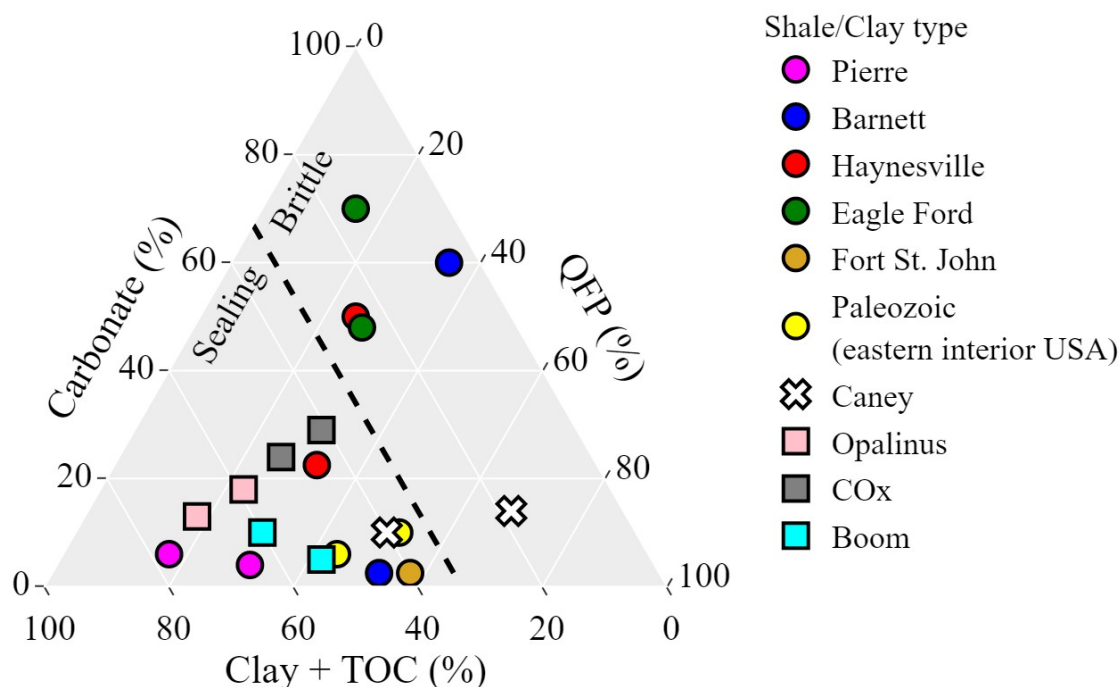


Figure 15 A ternary plot showing the mineral compositions of shales and clays <sup>61</sup>, with the boundary dashed line between ‘sealing’ and ‘brittle’ shales <sup>60</sup>. The circles indicate shales, whereas the squares clays. The Caney shale, which was modeled in this study, is represented by the ‘x’ symbols.

## 5. Conclusions

This research investigated the effect of shale creep on long-term integrity of a geological nuclear waste repository by conducting numerical simulations with a thermo-hydromechanically coupled code, TOUGH-FLAC, with the aim of identifying potential advantages of constructing repositories in shale with different creep properties. Creep deformations in shale were simulated with the Norton-Bailey creep model that was implemented in FLAC3D as a user-defined constitutive model. The parameters of the

Norton-Bailey model were calibrated against laboratory experiments to obtain a contrasting pair of shale creep properties: high and low creep shale cases. The temperature-dependence of shale creep was included in the Norton-Bailey model so that the effect of heating from radioactive nuclear wastes on shale creep is accounted for. The following findings were obtained from the results of this research:

- Deviatoric stresses in the formation decreased due to shale creep (i.e., high creep shale case) by as much as 100% relative to the baseline, no creep scenario at 100 years, whereas they decreased by only roughly 50% even at 10,000 years if the formation crept less (i.e., low creep shale case). In addition, the maximum deviatoric stress developed in the high creep shale was half that in the low creep shale because the stiffness of the high creep shale was 2.6 times less than that of the low creep shale. The high creep shale also dissipated stress concentrations around the tunnel. Hence, the more creep-prone the shale was, the greater the stress decreases and the more uniform the stress distributions in the formation became.
- The high creep shale developed orders of magnitude less permeability in the formation around the disposal tunnel (compared to the low creep shale) both in the short (i.e., 100 years) and long term (i.e., 10,000 years). However, in the intermediate term (i.e., 1,000 years), the permeability levels were similar between the two shale cases due to the simultaneous decreases in the mean effective stress (which increase the permeability) and increases in the deviatoric stress (which also increase the permeability) in the high creep shale case. Hence, although shale creep could increase formation integrity in the short and long term, it may not significantly improve the formation integrity in the intermediate term.



- The mean effective stress in the bentonite buffer decreased to just 2 MPa at 1,000 years due to creep-induced total stress plateau in the surrounding formation (i.e., high creep shale case), but it increased to 7 MPa at 10,000 years due to creep-induced contraction of the disposal tunnel. In the low creep shale case, on the other hand, the mean effective stress was 4 MPa at 1,000 years, but it gradually decreased to 3 MPa at 10,000 years because of the lack of creep-induced tunnel contraction. Thus, high creep shale could achieve better buffer integrity in the long-term (i.e., 10,000 years) while potentially degrading it in the intermediate-term (i.e., 1,000 years), whereas the opposite would be the case with low creep shale. It is noted that the short-term (i.e., 100 years) buffer integrity was not significantly affected by shale creep as the mean effective stress levels were similar in both shale cases (~5 MPa).

This research focused on stress- and temperature-dependent creep of shale, but some creep mechanisms such as creep due to shale grain-pore fluid interaction were not modeled explicitly. In order to address such creep mechanism in shale, thermo-hydromechanical-chemically (THMC) coupled simulations need to be performed. A THMC simulation could model the interaction between shale and radionuclides and thereby its effect on shale creep. Also, this research focused on the modeling under the 2D plane-strain condition, but a full 3D simulation, which could model deformations near the ground surface more accurately than the 2D simulation, may be conducted to consider 3D effects. In addition, material and/or structural anisotropy, such as bedding, may be incorporated into creep model parameters (after relevant experimental data become available) to consider their effects on the integrity of geological nuclear waste repositories in shales. Finally, an advanced viscoplastic model with a yield and/or failure locus may be employed to address the risk of failure during creep in the near-field formation in future studies.

## Acknowledgements

813 Funding was provided by the Spent Fuel and Waste Science and Technology, Office of Nuclear Energy,  
814 of the U.S. Department of Energy under Contract Number DE-AC02-05CH11231 with Lawrence  
815 Berkeley National Laboratory.

816

## 817 **References**

- 818 1. IAEA. *Scientific and Technical Basis for the Geological Disposal of Radioactive Wastes.*; 2003.  
819 [https://www.iaea.org/publications/6568/scientific-and-technical-basis-for-the-geological-disposal-](https://www.iaea.org/publications/6568/scientific-and-technical-basis-for-the-geological-disposal-of-radioactive-wastes)  
820 [of-radioactive-wastes](https://www.iaea.org/publications/6568/scientific-and-technical-basis-for-the-geological-disposal-of-radioactive-wastes)
- 821 2. Apted M, Ahn J. *Geological Repository Systems for Safe Disposal of Spent Nuclear Fuels and*  
822 *Radioactive Waste*. 1st Ed. Woodhead Publishing; 2010.  
823 [https://www.elsevier.com/books/geological-repository-systems-for-safe-disposal-of-spent-nuclear-](https://www.elsevier.com/books/geological-repository-systems-for-safe-disposal-of-spent-nuclear-fuels-and-radioactive-waste/apted/978-1-84569-542-2)  
824 [fuels-and-radioactive-waste/apted/978-1-84569-542-2](https://www.elsevier.com/books/geological-repository-systems-for-safe-disposal-of-spent-nuclear-fuels-and-radioactive-waste/apted/978-1-84569-542-2)
- 825 3. Rutqvist J. Coupled Thermo-Hydro-Mechanical Behavior of Natural and Engineered Clay  
826 Barriers. In: Tournassat C, Steefel C, Bourg I, Bergaya F, eds. *Natural and Engineered Clay*  
827 *Barriers*. Elsevier; 2015:329-355. [https://www.elsevier.com/books/natural-and-engineered-clay-](https://www.elsevier.com/books/natural-and-engineered-clay-barriers/tournassat/978-0-08-100027-4)  
828 [barriers/tournassat/978-0-08-100027-4](https://www.elsevier.com/books/natural-and-engineered-clay-barriers/tournassat/978-0-08-100027-4)
- 829 4. Tsang CF, Bernier F, Davies C. Geohydronechanical processes in the Excavation Damaged Zone  
830 in crystalline rock, rock salt, and indurated and plastic clays - In the context of radioactive waste  
831 disposal. *Int J Rock Mech Min Sci*. 2005;42(1):109-125. doi:10.1016/j.ijrmms.2004.08.003
- 832 5. Tsang C-F. Introduction to coupled processes. In: Tsang C-F, ed. *Coupled Processes Associated*  
833 *with Nuclear Waste Repositories*. Academic Press; 1987:1-6.  
834 <https://www.elsevier.com/books/coupled-processes-associated-with-nuclear-waste-repositories/>

tsang/978-0-12-701620-7

6. Blümling P, Bernier F, Lebon P, Derek Martin C. The excavation damaged zone in clay formations time-dependent behaviour and influence on performance assessment. *Phys Chem Earth*. 2007;32:588-599. doi:10.1016/j.pce.2006.04.034
7. Bechthold W, Rothfuchs T, Poley A, et al. *Backfilling and Sealing of Underground Repositories for Radioactive Waste in Salt (BAMBUS Project)*.; 1999. <https://op.europa.eu/en/publication-detail/-/publication/49ae90df-e3a6-4bd5-b55e-e505a9a15753>
8. Bossart P, Meier PM, Moeri A, Trick T, Mayor JC. Geological and hydraulic characterisation of the excavation disturbed zone in the Opalinus Clay of the Mont Terri Rock Laboratory. *Eng Geol*. 2002;66(1-2):19-38. doi:10.1016/S0013-7952(01)00140-5
9. Conil N, Vitel M, Plua C, Vu MN, Seyedi D, Armand G. In Situ Investigation of the THM Behavior of the Callovo-Oxfordian Claystone. *Rock Mech Rock Eng*. 2020;53(6):2747-2769. doi:10.1007/s00603-020-02073-8
10. Yu L, Weetjens E, Sillen X, et al. Consequences of the thermal transient on the evolution of the damaged zone around a repository for heat-emitting high-level radioactive waste in a clay formation: A performance assessment perspective. *Rock Mech Rock Eng*. 2014;47(1):3-19. doi:10.1007/s00603-013-0409-4
11. Thomas HR, Vardon PJ, Cleall PJ. Three-dimensional behaviour of a prototype radioactive waste repository in fractured granitic rock. *Can Geotech J*. 2014;51(4):246-259. doi:10.1139/cgj-2013-0094
12. Sasaki T, Rutqvist J. Estimation of stress and stress-induced permeability change in a geological nuclear waste repository in a thermo-hydrologically coupled simulation. *Comput Geotech*.

2021;129(October 2020):103866. doi:10.1016/j.compgeo.2020.103866

13. Rutqvist J, Zheng L, Chen F, Liu HH, Birkholzer J. Modeling of coupled thermo-hydro-mechanical processes with links to geochemistry associated with bentonite-backfilled repository tunnels in clay formations. *Rock Mech Rock Eng.* 2014;47(1):167-186. doi:10.1007/s00603-013-0375-x

14. Rutqvist J. Thermal management associated with geologic disposal of large spent nuclear fuel canisters in tunnels with thermally engineered backfill. *Tunn Undergr Sp Technol.* 2020;102(April):103454. doi:10.1016/j.tust.2020.103454

15. Blanco-Martín L, Rutqvist J, Birkholzer JT. Long-term modeling of the thermal-hydraulic-mechanical response of a generic salt repository for heat-generating nuclear waste. *Eng Geol.* 2015;193:198-211. doi:10.1016/j.enggeo.2015.04.014

16. Blanco-Martín L, Wolters R, Rutqvist J, Lux KH, Birkholzer JT. Comparison of two simulators to investigate thermal-hydraulic-mechanical processes related to nuclear waste isolation in saliferous formations. *Comput Geotech.* 2015;66:219-229. doi:10.1016/j.compgeo.2015.01.021

17. Blanco-Martín L, Rutqvist J, Battistelli A, Birkholzer JT. Coupled Processes Modeling in Rock Salt and Crushed Salt Including Halite Solubility Constraints: Application to Disposal of Heat-Generating Nuclear Waste. *Transp Porous Media.* 2018;124(1):159-182. doi:10.1007/s11242-018-1057-7

18. Zhang Q, Fink R, Krooss B, Jalali M, Littke R. Reduction of shale permeability by temperature-induced creep. *SPE J.* 2021;26(2):750-764. doi:10.2118/204467-PA

19. Benge M, Lu Y, Katende A, et al. Connecting Geomechanical Properties with Potential for Proppant Embedment and Production Decline for the Emerging Caney Shale , Oklahoma. In:

- 879 *Unconventional Resources Technology Conference.* ; 2021. doi:10.15530/urtec-2021-1234
- 880 20. Sone H, Zoback MD. Visco-plastic properties of shale gas reservoir rocks. In: *45th US Rock*  
881 *Mechanics / Geomechanics Symposium.* ; 2011. [https://onepetro.org/ARMAUSRMS/proceedings-](https://onepetro.org/ARMAUSRMS/proceedings-abstract/ARMA11/All-ARMA11/ARMA-11-417/120373)  
882 [abstract/ARMA11/All-ARMA11/ARMA-11-417/120373](https://onepetro.org/ARMAUSRMS/proceedings-abstract/ARMA11/All-ARMA11/ARMA-11-417/120373)
- 883 21. Nopola JR, Roberts LA. Time-dependent deformation of Pierre Shale as determined by long-  
884 duration creep tests. In: *50th US Rock Mechanics / Geomechanics Symposium.* ; 2016:584-591.  
885 [https://onepetro.org/ARMAUSRMS/proceedings-abstract/ARMA16/All-ARMA16/ARMA-2016-](https://onepetro.org/ARMAUSRMS/proceedings-abstract/ARMA16/All-ARMA16/ARMA-2016-508/126299)  
886 [508/126299](https://onepetro.org/ARMAUSRMS/proceedings-abstract/ARMA16/All-ARMA16/ARMA-2016-508/126299)
- 887 22. Li Y, Ghassemi A. Creep behavior of Barnett, Haynesville, and Marcellus shale. In: *46th US Rock*  
888 *Mechanics / Geomechanics Symposium.* ; 2012:641-647.  
889 [https://onepetro.org/ARMAUSRMS/proceedings-abstract/ARMA12/All-ARMA12/ARMA-2012-](https://onepetro.org/ARMAUSRMS/proceedings-abstract/ARMA12/All-ARMA12/ARMA-2012-330/120741)  
890 [330/120741](https://onepetro.org/ARMAUSRMS/proceedings-abstract/ARMA12/All-ARMA12/ARMA-2012-330/120741)
- 891 23. Rybacki E, Herrmann J, Wirth R, Dresen G. Creep of Posidonia Shale at Elevated Pressure and  
892 Temperature. *Rock Mech Rock Eng.* 2017;50(12):3121-3140. doi:10.1007/s00603-017-1295-y
- 893 24. Liang Z, Chen Z, Rahman SS. Experimental investigation of the primary and secondary creep  
894 behaviour of shale gas reservoir rocks from deep sections of the Cooper Basin. *J Nat Gas Sci Eng.*  
895 2020;73(September 2019):103044. doi:10.1016/j.jngse.2019.103044
- 896 25. Rutqvist J. Status of the TOUGH-FLAC simulator and recent applications related to coupled fluid  
897 flow and crustal deformations. *Comput Geosci.* 2011;37(6):739-750.  
898 doi:10.1016/j.cageo.2010.08.006
- 899 26. Rinaldi AP, Rutqvist J, Luu K, Blanco-Martín L, Hu M, Sentís ML. TOUGH3-FLAC3D: A  
900 MODELING APPROACH FOR PARALLEL COMPUTING OF FLUID FLOW AND

901 GEOMECHANICS [Preprint]. *Earth Sp Sci Open Arch*. Published online 2021.  
 902 <https://doi.org/10.1002/essoar.10505967.1>

903 27. Jung Y, Shu Heng Pau G, Finsterle S, Doughty C. *TOUGH3 User's Guide.*; 2018.  
 904 [https://tough.lbl.gov/assets/files/Tough3/TOUGH3\\_Users\\_Guide\\_v2.pdf](https://tough.lbl.gov/assets/files/Tough3/TOUGH3_Users_Guide_v2.pdf)

905 28. Itasca Consulting Group. *FLAC3D — Fast Lagrangian Analysis of Continua in Three-*  
 906 *Dimensions, Ver. 7.0.*; 2020. <https://www.itascacg.com/software/FLAC3D>

907 29. Rutqvist J, Wu Y-S, Tsang C-F, Bodvarsson G. A modeling approach for analysis of coupled  
 908 multiphase fluid flow, heat transfer, and deformation in fractured porous rock. *Int J Rock Mech Min*  
 909 *Sci*. 2002;39(4):429-442. doi:10.1016/S1365-1609(02)00022-9

910 30. van Genuchten MT. A Closed-form Equation for Predicting the Hydraulic Conductivity of  
 911 Unsaturated Soils1. *Soil Sci Soc Am J*. 1980;44(5):892.  
 912 doi:10.2136/sssaj1980.03615995004400050002x

913 31. Herrmann J, Rybacki E, Sone H, Dresen G. Deformation Experiments on Bowland and Posidonia  
 914 Shale—Part II: Creep Behavior at In Situ p c–T Conditions. *Rock Mech Rock Eng*.  
 915 2020;53(2):755-779. doi:10.1007/s00603-019-01941-2

916 32. Saxena N, Mavko G, Zoback M, Hofmann R, Braunsdorf N. Joint estimation of acoustic  
 917 properties, creep, and stress relaxation in organic-rich shales. In: *SEG New Orleans Annual*  
 918 *Meeting.* ; 2015:3053-3057. doi:10.1190/segam2015-5874987.1

919 33. Hagin PN, Zoback MD. Inverting for creep strain parameters of uncemented reservoir sands using  
 920 arbitrary stress-strain data. In: *44th US Rock Mechanics Symposium - 5th US/Canada Rock*  
 921 *Mechanics Symposium.* ; 2010.  
 922 [61](https://onepetro.org/ARMAUSRMS/proceedings-abstract/ARMA10/All-ARMA10/ARMA-10-</a></p>
</div>
<div data-bbox=)

923 171/119372

924 34. Sone H, Zoback MD. Time-dependent deformation of shale gas reservoir rocks and its long-term  
925 effect on the in situ state of stress. *Int J Rock Mech Min Sci*. 2014;69:120-132.  
926 doi:10.1016/j.ijrmms.2014.04.002

927 35. Geng Z, Bonnelye A, Chen M, et al. Time and Temperature Dependent Creep in Tournemire  
928 Shale. *J Geophys Res Solid Earth*. 2018;123(11):9658-9675. doi:10.1029/2018JB016169

929 36. Sone H, Zoback MD. Time-dependent deformation of shale gas reservoir rocks and its long-term  
930 effect on the in situ state of stress. *Int J Rock Mech Min Sci*. 2014;69:120-132.  
931 doi:10.1016/j.ijrmms.2014.04.002

932 37. Norton FH. *Creep of Steel at High Temperatures*. McGraw-Hill; 1929.  
933 <https://archive.org/details/creepofsteelathi00nort/page/66/mode/2up?ref=ol&view=theater>

934 38. Bailey RW. The Utilization of Creep Test Data in Engineering Design. *Proc Inst Mech Eng*.  
935 1935;131(1):131-349. [https://doi.org/10.1243/pime\\_proc\\_1935\\_131\\_012\\_02](https://doi.org/10.1243/pime_proc_1935_131_012_02)

936 39. COMSOL. *Structural Mechanics Module User's Guide*. COMSOL Multiphysics® v. 6.0.  
937 COMSOL AB; 2021.  
938 [https://doc.comsol.com/6.0/docserver/#!/com.comsol.help.sme/sme\\_ug\\_theory.06.33.html](https://doc.comsol.com/6.0/docserver/#!/com.comsol.help.sme/sme_ug_theory.06.33.html)

939 40. Lemaître J. *Sur La Détermination Des Lois de Comportement Des Matériaux Élasto-Visco-*  
940 *Plastiques*. Vol 135.; 1970.  
941 [https://books.google.com/books/about/Sur\\_la\\_détermination\\_des\\_lois\\_de\\_compor.html?](https://books.google.com/books/about/Sur_la_détermination_des_lois_de_compor.html?id=iFq0nAEACAAJ)  
942 [id=iFq0nAEACAAJ](https://books.google.com/books/about/Sur_la_détermination_des_lois_de_compor.html?id=iFq0nAEACAAJ)

943 41. Menzel W, Schreiner W. Zum geomechanischen Verhalten von Steinsalz verschiedener  
944 Lagerstätten der DDR. Teil II: Das Verformungsverhalten. *Neue Bergbautechnik*. 1977;7(8):565–

- 945 574. [https://scholar.google.com/scholar\\_lookup?title=Zum geomechanischen Verhalten von](https://scholar.google.com/scholar_lookup?title=Zum+geomechanischen+Verhalten+von+Steinsalz+verschiedener+Lagersttten+der+DDR.+Teil+II%3A+Das+Verformungsverhalten&journal=Neue+Bergbautechnik&volume=7&pages=565-574&publication_year=1977&author=Menzel%2CW.)  
946 Steinsalz verschiedener Lagersttten der DDR. Teil II%3A Das  
947 Verformungsverhalten&journal=Neue Bergbautechnik&volume=7&pages=565-  
948 574&publication\_year=1977&author=Menzel%2CW.
- 949 42. Kazmierczak JB, Laouafa F, Ghoreychi M, Lebon P, Barnichon JD. Influence of creep on water  
950 pressure measured from borehole tests in the Meuse/Haute-Marne Callovo-Oxfordian argillites.  
951 *Phys Chem Earth*. 2007;32(8-14):917-921. doi:10.1016/j.pce.2006.01.008
- 952 43. Gens A, Alonso EE. A framework for the behaviour of unsaturated expansive clays. *Can Geotech*  
953 *J*. 1992;29(6):1013-1032. <https://doi.org/10.1139/t92-120>
- 954 44. Rutqvist J, Ijiri Y, Yamamoto H. Implementation of the Barcelona Basic Model into TOUGH-  
955 FLAC for simulations of the geomechanical behavior of unsaturated soils. *Comput Geosci*.  
956 2011;37(6):751-762. doi:10.1016/j.cageo.2010.10.011
- 957 45. Gens A, Snchez M, Guimares LDN, et al. A full-scale in situ heating test for high-level nuclear  
958 waste disposal: Observations, analysis and interpretation. *Geotechnique*. 2009;59(4):377-399.  
959 doi:10.1680/geot.2009.59.4.377
- 960 46. Chang C, Zoback MD. Viscous creep in room-dried unconsolidated Gulf of Mexico shale (I):  
961 Experimental results. *J Pet Sci Eng*. 2009;69(3-4):239-246. doi:10.1016/j.petrol.2009.08.018
- 962 47. Mighani S, Taneja S, Sondergeld CH, Rai CS. Nanoindentation creep measurements on shale. In:  
963 *49th US Rock Mechanics / Geomechanics Symposium*. ; 2015.  
964 [https://onepetro.org/ARMAUSRMS/proceedings-abstract/ARMA15/All-ARMA15/ARMA-2015-](https://onepetro.org/ARMAUSRMS/proceedings-abstract/ARMA15/All-ARMA15/ARMA-2015-148/65018)  
965 148/65018
- 966 48. Sone H, Zoback M. Mechanical properties of shale-gas reservoir rocks — Part 2: Ductile creep,



- 967 brittle strength, and their relation to the elastic modulus. *Geophysics*. 2013;78(5):D393-D402.  
 968 doi:10.1190/geo2013-0051.1
- 969 49. Kawabata K, Tanaka H, Kitamura Y, Ma KF. Apparent activation energy and rate-limiting process  
 970 estimation from natural shale deformed by pressure solution in shallow subduction zone. *Earth*  
 971 *Planet Sci Lett*. 2009;287(1-2):57-63. doi:10.1016/j.epsl.2009.07.032
- 972 50. Rutqvist J, Borgegson L, Chijimatsu M, et al. Modeling of damage, permeability changes and  
 973 pressure responses during excavation of the TSX tunnel in granitic rock at URL, Canada. *Environ*  
 974 *Geol*. 2009;57(6):1263-1274. doi:10.1007/s00254-008-1515-6
- 975 51. Pardoën B. Hydro-mechanical analysis of the fracturing induced by the excavation of nuclear  
 976 waste repository galleries using shear banding. Published online 2015.  
 977 <https://orbi.uliege.be/handle/2268/188222>
- 978 52. Chang C, Zoback MD. Viscous creep in room-dried unconsolidated Gulf of Mexico shale (II):  
 979 Development of a viscoplasticity model. *J Pet Sci Eng*. 2010;72(1-2):50-55.  
 980 doi:10.1016/j.petrol.2010.03.002
- 981 53. Hagin PN, Zoback MD. Viscoplastic deformation in unconsolidated reservoir sands (Part 1):  
 982 Laboratory observations and time-dependent end cap models. In: *6th North America Rock*  
 983 *Mechanics Symposium (NARMS)*. ; 2004. [https://onepetro.org/ARMANARMS/proceedings-](https://onepetro.org/ARMANARMS/proceedings-abstract/ARMA04/All-ARMA04/ARMA-04-567/117636)  
 984 [abstract/ARMA04/All-ARMA04/ARMA-04-567/117636](https://onepetro.org/ARMANARMS/proceedings-abstract/ARMA04/All-ARMA04/ARMA-04-567/117636)
- 985 54. Fabre G, Pellet F. Creep and time-dependent damage in argillaceous rocks. *Int J Rock Mech Min*  
 986 *Sci*. 2006;43(6):950-960. doi:10.1016/j.ijrmms.2006.02.004
- 987 55. Almasoodi MM, Abousleiman YN, Hoang SK. Viscoelastic Creep of Eagle Ford Shale :  
 988 Investigating Fluid-Shale Interaction. In: *SPE/CSUR Unconventional Resources Conference*. ;

989 2014. [https://onepetro.org/SPEURCC/proceedings-abstract/14URCC/3-14URCC/](https://onepetro.org/SPEURCC/proceedings-abstract/14URCC/3-14URCC/D031S011R002/212340)  
990 D031S011R002/212340

991 56. Heller RJ, Zoback MD. Adsorption, swelling and viscous creep of synthetic clay samples. In: *45th*  
992 *US Rock Mechanics / Geomechanics Symposium.* ; 2011.  
993 [https://onepetro.org/ARMAUSRMS/proceedings-abstract/ARMA11/All-ARMA11/ARMA-11-](https://onepetro.org/ARMAUSRMS/proceedings-abstract/ARMA11/All-ARMA11/ARMA-11-469/120393)  
994 469/120393

995 57. Hol S, Zoback MD. Creep behavior of coal and shale related to adsorption of reservoir fluids. In:  
996 *47th US Rock Mechanics / Geomechanics Symposium.* ; 2013.  
997 [https://onepetro.org/ARMAUSRMS/proceedings-abstract/ARMA13/All-ARMA13/ARMA-2013-](https://onepetro.org/ARMAUSRMS/proceedings-abstract/ARMA13/All-ARMA13/ARMA-2013-556/121045)  
998 556/121045

999 58. Marschall P, Giger S, De La Vassière R, et al. Hydro-mechanical evolution of the EDZ as  
1000 transport path for radionuclides and gas: insights from the Mont Terri rock laboratory  
1001 (Switzerland). *Swiss J Geosci.* 2017;110(1):173-194. doi:10.1007/s00015-016-0246-z

1002 59. Katende A, Rutqvist J, Bengtson M, et al. Convergence of micro-geochemistry and micro-  
1003 geomechanics towards understanding proppant shale rock interaction: A Caney shale case study in  
1004 southern Oklahoma, USA. *J Nat Gas Sci Eng.* 2021;96(September):104296.  
1005 doi:10.1016/j.jngse.2021.104296

1006 60. Bourg IC. Sealing Shales versus Brittle Shales: A Sharp Threshold in the Material Properties and  
1007 Energy Technology Uses of Fine-Grained Sedimentary Rocks. *Environ Sci Technol Lett.*  
1008 2015;2(10):255-259. doi:10.1021/acs.estlett.5b00233

1009 61. Stein E, Bryan C, Dobson D, et al. *Disposal Concepts for a High-Temperature Repository in*  
1010 *Shale.*; 2020. doi:10.2172/1714419

